

Discrete Eigenseparation-based Reduced Order Homogenization Method for Failure Modeling of Composite Materials

Caglar Oskay*, Zimu Su and Berkcan Kapusuzoglu

Department of Civil and Environmental Engineering
Vanderbilt University
Nashville, TN 37235

Abstract

This manuscript presents a new reduced order computational homogenization method for failure analysis of composite materials. The proposed approach relies on the discrete representation of the fracture process at the fine scale that consistently bridges to a continuum representation of damage at the coarse scale. In order to achieve very high computational efficiency, the proposed approach builds on the ideas of the eigendeformation-based reduced order homogenization method, but tracks microscale failure evolution over a set of discrete cohesive failure surfaces. The formulation concurrently achieves mesh size objectivity and multiscale consistency by establishing analytical relationships between the microstructure size and the macroscale element size. The performance of the proposed formulation is demonstrated in the context of three-dimensional, laminated fiber reinforced composite configurations. The numerical experiments demonstrate mesh size objectivity in the presence of multiscale failure mechanisms including fiber fracture and transverse matrix cracking.

Keywords: Multiscale modeling; Fracture; Computational homogenization; Reduced order modeling.

1 Introduction

Failure prediction in composites materials is of significant interest since these materials are being increasingly deployed in various engineering applications at or near their limit states to maximize weight reduction or performance. Multiscale computational methods provide a rigorous framework and a strong mathematical basis for failure prediction in composites and holds

*Corresponding author address: VU Station B#351831, 2301 Vanderbilt Place, Nashville, TN 37235. Email: caglar.oskay@vanderbilt.edu

significant promise. While a number of multiscale methodologies such as the heterogeneous multiscale method [1], multiscale finite element method [2], variational multiscale enrichment and other numerical subgrid methods [3–6] are available and could be adopted for failure modeling, the present work focuses on the computational homogenization method (CH) [7, 8]. The adoption of CH for failure prediction requires overcoming a number of computational challenges. For instance, when progressive failure is described using the continuum damage mechanics approach, localization limiters must be employed at all relevant scales to ensure mesh objectivity. Regardless of continuum or discrete representation of failure, consistent bridging of failure information across scales (i.e., homogenization and localization operators) must be established. In the presence of localization of damage, statistical homogeneity and ergodicity at the scale of the microstructure is lost and a representative volume element (RVE) cannot be defined [9]. An additional, no less critical challenge is that the computational cost associated with evaluating multiple nested numerical problems that involve failure and fracture processes is typically computationally prohibitive beyond small problems of academic relevance. In the past decade, significant effort has been therefore devoted to alleviate the above-mentioned computational challenges.

A number of early studies focused on applying computational homogenization principles to address problems, where fracture is localized to material interfaces (see e.g., [10, 11]). The applicability and generality of CH to address fracture problems has been further extended since then. The formulations of CH for fracture typically differ slightly according to the type of representation of failure at the fine and coarse scales. Discrete-discrete (for fine and coarse scales respectively), continuum-discrete and continuum-continuum representations have been proposed. From the algorithmic standpoint, the work by Belytschko et al. [12] is of significance as it introduced the concept of microstructural domain splitting to bridge the fracture process and the bulk behavior separately across scales. The idea has been employed by a number of others since then. Verhoosel et al. [13] introduced the methodology to link the progressive evolution (i.e., cohesive cracks) of macroscopic interfacial and bulk cracks to the corresponding microscopic processes in the discrete-discrete sense. This approach was later extended to continuum-discrete failure representations [14, 15]. Coenen et al. [16] introduced a methodology to perform bulk and discontinuity upscaling without the need for microstructure domain splitting. Bosco et al. [17] extended this methodology to account for strain discontinuities across the macroscale crack surface. A computational framework similar to above that includes strong discontinuity enrichment has been developed in Refs. [18, 19].

Extending CH to problems where failure at the coarse scale is modeled in a continuum setting typically requires a different treatment to achieve objective formulations. One approach is to explicitly treat the coarse scale problem using a nonlocal formulation (e.g., gradient or integral type localization limiter [20, 21]). Kouznetsova et al. [22] proposed a gradient enhanced

CH theory to study localization problems where the characteristic length of localization is larger than the microstructure size. Oliver et al. [23] proposed a multiscale approach, where failure at each scale is represented using the continuum strong discontinuity approach. Leveraging their earlier work on RVE existence, Gitman et al. [24] proposed an alternative scale bridging strategy, in which the RVE size is tied to the macroscale finite element size for regularization, named the couple volume approach. An idea similar to the couple volume approach is employed in the current study.

While the elegant theories mentioned above provide a consistent upscaling strategy in the presence of nucleation and propagation of failure, they are often computationally too costly for application to problems that involve large structures. Due to this limitation, a significant majority (if not all) of these approaches has been applied in 2-D problems. The issue of high computational cost can be alleviated based on either surrogate modeling (e.g., machine learning [25–27]) or basis reduction strategies to approximate the response at the scale of the microstructure. In the context of nonlinear behavior of composites, a number of methodologies have been proposed, including generalized method of cells [28], proper orthogonal decomposition [29], proper generalized decomposition [30], fast Fourier transform [31], transformation field analysis [32, 33] and eigendeformation-based homogenization [34–36], among others. Despite significant progress in this domain, consistent formulations that address all complications arising from treatment of material softening or crack propagation in multiscale formulations have been rare. Oliver et al. [37] recently proposed a model order reduction methodology that builds on the continuum strong discontinuity approach to accelerate multiscale failure simulations in random composites. In addition to basis reduction techniques and particularly in conjunction with it, massive parallelization [38], effective linear [39] and nonlinear [40] solver methodologies, adaptive/selective multiscale representation within the problem domain offer additional approaches for accelerated multiscale computations.

In this manuscript, we present a new reduced order computational homogenization approach for failure analysis of composite materials. The proposed approach relies on the discrete representation of the fracture process at the fine scale that consistently bridges to a continuum representation of damage at the coarse scale. The choice of discrete-continuum representation is motivated by experimental observations in fiber reinforced polymer composites, where a few distinct cracks morphologies and orientations observed at the microstructure scale culminates to diffuse damage patterns at the macroscale. The proposed approach builds on the ideas of the Eigendeformation-based reduced order Homogenization Method (EHM) [35], but introduces the following novel contributions:

1. The evolution of damage at the microscale is tracked over a set of discrete cohesive “potential” failure surfaces (i.e., failure paths) defined over surface morphologies and

represented using a reduced approximation basis. This is in contrast to the classical EHM, where volume-based failure paths define the progressive damage evolution idealized using continuum damage.

2. Leveraging the surface-based representation of failure, the fracture process is expressed in terms of experimentally-measurable fracture metrics, such as the fracture energy and cohesive strength.
3. The proposed formulation alleviates mesh size sensitivity and concurrently achieves mesh objectivity and multiscale consistency by establishing analytical relationships between the microstructure size and the macroscale element size.

The performance of the proposed formulation is demonstrated using laminated fiber reinforced composite configurations. The numerical experiments demonstrate mesh size objectivity in the presence of multiscale failure mechanisms including fiber fracture and transverse matrix cracking in the context of three-dimensional configurations.

The remainder of this manuscript is organized as follows: In Section 2, the formulation of the proposed modeling approach, the treatment of multiple and possibly intersecting failure paths, the basis reduction approach and the treatment of mesh size objectivity are discussed. The details of the numerical implementation of the D-EHM model is presented in Section 3. Section 4 provides the verification of the proposed approach in the context of unnotched and notched laminated composite configurations. Section 5 discusses the summary and conclusions. An appendix is included that provides the detailed formulation of the coefficient tensor scaling for mesh size objectivity.

2 Discrete EHM Formulation

Consider a heterogeneous structure that occupies a domain, $\Omega \subset \mathbb{R}^{n_{sd}}$, where $n_{sd} = 2, 3$ is the number of spatial dimensions. The body is made of a periodic arrangement of a microstructural volume. In the absence of failure processes, the microstructure volume is defined by a statistically representative volume element (RVE), a statistical volume element (SVE) or a unit cell (UC). In the presence of the failure process, the RVE concept is no longer valid. In this manuscript, the microstructure volume is chosen large enough to adequately represent the geometrical features of the material composition and denoted as $\Theta \subset \mathbb{R}^{n_{sd}}$. The microstructure typically consists of two or more material constituents, but reticulated single material morphologies are also admissible. Under the applied loading, the structure undergoes brittle or quasi-brittle fracture. While it is possible to include nonlinear, path dependent deformation within the material constituents, these effects are ignored and we focus our attention to modeling of the fracture events in otherwise elastic constituents. Due to the geometrical

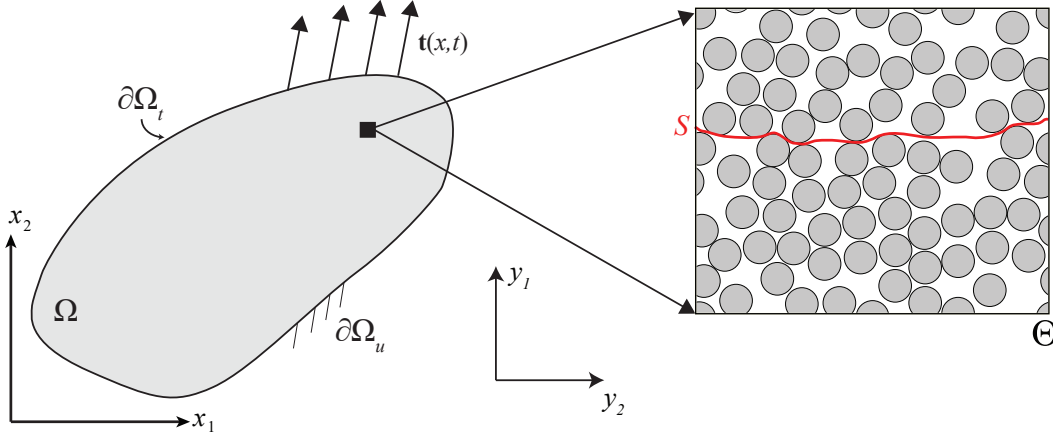


Figure 1: Multiple spatial scales.

arrangement of the constituents at the micro- or mesoscales (e.g., laminated configurations of a unidirectionally reinforced composite), the fracture patterns within the structure could be complex and diffuse.

The proposed approach is based on the computational homogenization method with multi-scale spatial scales [41]. The macroscopic and the microstructural domains are parameterized using position coordinates, \mathbf{x} and \mathbf{y} , respectively (Fig. 1). The two scales are related to each other by the scaling parameter, $0 < \zeta \ll 1$ such that $\mathbf{y}(\mathbf{x}) = \mathbf{x}/\zeta$, and the response fields (e.g., displacement, stress, strain) are expressed as a function of the micro- and macroscopic coordinates. The governing equations of the boundary value problems that describe the nonlinear deformation processes at the micro- and macroscopic scales are obtained through a two-scale asymptotic analysis, the details of which are available in the literature and skipped herein for brevity [7, 8, 41].

We focus our attention to a progressively damaging microstructure at an arbitrary macroscopic position, $\mathbf{x} \in \Omega$. The displacement field over the microstructure, \mathbf{u} is expressed in terms of a two-scale asymptotic decomposition:

$$\mathbf{u}(\mathbf{x}, \mathbf{y}, t) = \mathbf{u}^0(\mathbf{x}, t) + \zeta \mathbf{u}^1(\mathbf{x}, \mathbf{y}, t) \quad (1)$$

The leading order displacement field \mathbf{u}^0 is continuous and constant across the microstructure. Under the applied loading, a microcrack nucleates and forms within the microstructure (Fig. 1) resulting in a displacement jump discontinuity (i.e., separation), $\delta(\mathbf{x}, \mathbf{y}, t) := \llbracket \mathbf{u}^1 \rrbracket$ along a discontinuity path, $\mathbf{y} \in S \subset \mathbb{R}^{n_{sd}-1}$ as illustrated in Fig. 1. The microscale displacement field \mathbf{u}^1 and the separation δ are taken to be periodic over the microstructure and their contribution to the overall displacement field is of $O(\zeta)$. It is also possible to consider different boundary conditions such as that suggested in Ref. [42–44]. Our approach to localize the

jump discontinuity leveraging the periodicity condition are further discussed in Section 2.3. Employing the concept of eigen-separations [35] and the classical arguments of mathematical homogenization, the microstructural displacement field is expressed as:

$$\mathbf{u}^1(\mathbf{x}, \mathbf{y}, t) = \mathbf{H}(\mathbf{y}) : \boldsymbol{\epsilon}^0(\mathbf{x}, t) + (\mathbf{h} * \boldsymbol{\delta})_S(\mathbf{x}, \mathbf{y}, t) \quad (2)$$

where, $\boldsymbol{\epsilon}^0 = \nabla_{\mathbf{x}}^s \mathbf{u}^0$, $\nabla_{\mathbf{x}}^s$ is the symmetric gradient operator with respect to the macroscopic coordinates, considering the small strain theory, $\mathbf{H}(\mathbf{y})$ and $\mathbf{h}(\mathbf{y}, \hat{\mathbf{y}})$ are the elastic and separation influence functions of the microstructure, respectively, and $(\cdot * \cdot)_S$ denotes the convolution operation over the discontinuity path, S :

$$(\mathbf{h} * \boldsymbol{\delta})_S(\mathbf{x}, \mathbf{y}, t) = \int_S \mathbf{h}(\mathbf{y}, \hat{\mathbf{y}}) \cdot \boldsymbol{\delta}(\mathbf{x}, \hat{\mathbf{y}}) d\hat{\mathbf{y}} \quad (3)$$

In the absence of a fracture event (i.e., $\boldsymbol{\delta} = \mathbf{0}$), the formulation results in the classical elastic homogenization theory, where the third-order elastic influence function, \mathbf{H} provides the variation of the response over the microstructure volume. The numerical evaluation of \mathbf{H} is standard [7]. The second-order separation influence function \mathbf{h} is computed as responses to unit normal and tangential separations applied along the discontinuity path ($\hat{\mathbf{y}} \in S$). The numerical evaluation procedure to compute the separation influence function is provided in Ref. [35].

Employing the scaling relationship and taking the symmetric gradient of Eq. 1, the strain field over the microstructure is expressed as:

$$\boldsymbol{\epsilon}(\mathbf{x}, \mathbf{y}, t) = \boldsymbol{\epsilon}^0(\mathbf{x}, t) + \boldsymbol{\epsilon}_y^1(\mathbf{x}, \mathbf{y}, t) = \mathbf{A}(\mathbf{y})\boldsymbol{\epsilon}^0 + (\mathbf{g} * \boldsymbol{\delta})_S \quad (4)$$

in which, $\boldsymbol{\epsilon}_y^1 = \nabla_{\mathbf{y}}^s \mathbf{u}^1$, $\mathbf{A} = \mathbf{I} + \mathbf{G}$, \mathbf{I} is the fourth order identity tensor, $\mathbf{G} = \nabla_{\mathbf{y}}^s \mathbf{H}$ is the elastic polarization tensor, and $\mathbf{g} = \nabla_{\mathbf{y}}^s \mathbf{h}$ stands for the separation polarization tensor. The macroscopic strain, $\bar{\boldsymbol{\epsilon}}$ is obtained by averaging Eq. 4 over the domain of the microstructure:

$$\bar{\boldsymbol{\epsilon}}(\mathbf{x}, t) := \langle \boldsymbol{\epsilon} \rangle_{\Theta} = \boldsymbol{\epsilon}^0(\mathbf{x}, t) + \langle (\mathbf{g} * \boldsymbol{\delta})_S \rangle_{\Theta} \quad (5)$$

where, $\langle \cdot \rangle_{\Theta}$ denotes the volume (or surface) averaging operator with respect to the domain denoted in the subscript, $|\Theta|$ and $|S|$ are the volume of the microstructure and the surface area of the discontinuity path, respectively.

Equation 5 employs the continuity and periodicity of the elastic influence function, which implies that the elastic polarization function has null average. Unlike \mathbf{H} , the separation influence function is discontinuous across the discontinuity path, S . Nevertheless, it is straightforward to see that the second term in Eq. 5 vanishes (i.e., $\langle (\mathbf{g} * \boldsymbol{\delta})_S \rangle_{\Theta} = \langle (\mathbf{g})_{\Theta} * \boldsymbol{\delta} \rangle_S = \mathbf{0}$) and hence $\bar{\boldsymbol{\epsilon}} = \boldsymbol{\epsilon}^0$.

The microscale equilibrium equation defined over the microstructural volume is:

$$\nabla_{\mathbf{y}} \cdot \boldsymbol{\sigma}(\mathbf{x}, \mathbf{y}, t) = \nabla_{\mathbf{y}} \cdot (\mathbf{L}(\mathbf{y}) : \boldsymbol{\epsilon}) = \mathbf{0}; \quad \mathbf{y} \in \Theta \quad (6)$$

in which, $\boldsymbol{\sigma}$ denotes stress, and \mathbf{L} is the tensor of elastic moduli that varies within the microstructure due to the presence of multiple material constituents. Substituting Eqs. 4 and 5 into Eq. 6, premultiplying the resulting equation with the influence function, \mathbf{h} and integrating over the microstructure yields ($\forall \hat{\mathbf{y}} \in S$):

$$\mathbf{t}(\mathbf{x}, \hat{\mathbf{y}}, t) - \mathbf{C}(\hat{\mathbf{y}}) : \bar{\boldsymbol{\epsilon}} - \int_{\Theta} \mathbf{g}(\mathbf{y}, \hat{\mathbf{y}}) : \mathbf{L} : (\mathbf{g} * \boldsymbol{\delta})_S(\mathbf{x}, \mathbf{y}, t) d\mathbf{y} = \mathbf{0} \quad (7)$$

where, \mathbf{t} is the traction along the discontinuity path, and \mathbf{C} is a third order coefficient tensor:

$$\mathbf{C}(\hat{\mathbf{y}}) := \int_{\Theta} \mathbf{g}(\mathbf{y}, \hat{\mathbf{y}}) : \mathbf{L}(\mathbf{y}) : \mathbf{A}(\mathbf{y}) d\mathbf{y} \quad (8)$$

Equation 7 constitutes a weak equilibrium statement defined over the microstructure. The construction described above is equivalent to weighted residuals method with collocation over the discontinuity path and provides a relationship between the tractions and separations along the discontinuity path as a function of the macroscopic strain. The system of equations governing the microscale behavior is closed by employing a cohesive law, where the traction along the discontinuity path is expressed as a history dependent, nonlinear function of the separations:

$$\mathbf{t} = \hat{\mathbf{t}}(\boldsymbol{\delta}, \mathbf{q}) \quad (9)$$

in which, \mathbf{q} denote a vector of internal state variables that define the evolution of the cohesive law. The evolution laws for the internal state variables are material-specific and provided in Section 4 as a part of the numerical verifications.

Figure 2 provides the summary of the system of equations for the microscale boundary value problem obtained through classical computational homogenization and the alternative form of the microscale problem obtained using the eigen-separation concept. In the proposed formulation, the microstructural boundary value problem is defined over the discontinuity path, S instead of the microstructure domain, Θ .

2.1 Multiple Failure Paths

Within the heterogeneous structure, Ω with complex geometry and loading, cracks along different orientations may form at different parts of the domain, propagating cracks may change direction to follow a load path, or multiple cracks may form near each other and interact. In the context of the proposed D-EHM methodology, we consider the simultaneous presence of

<p><u>Classical microscale problem</u> ($\mathbf{y} \in \Theta$): Given: macroscale strain: $\bar{\epsilon}$; cohesive law and associated parameters and ISVs. Compute: microscale displacement: \mathbf{u}^1</p> <p>Equilibrium equation: $\nabla_{\mathbf{y}} \cdot \boldsymbol{\sigma}(\mathbf{x}, \mathbf{y}, t) = \mathbf{0}$</p> <p>Constitutive equation: $\boldsymbol{\sigma} = \mathbf{L}(\mathbf{y}) : (\bar{\epsilon}(\mathbf{x}, t) + \boldsymbol{\epsilon}_{\mathbf{y}}^1(\mathbf{x}, \mathbf{y}, t))$</p> <p>Cohesive behavior: $\mathbf{t} = \hat{\mathbf{t}}(\boldsymbol{\delta}, \mathbf{q}); \quad \mathbf{y} \in S$</p> <p>Boundary condition: \mathbf{u}^1 periodic on $\mathbf{y} \in \partial\Theta$</p>	<p><u>Eigenseparation form</u> ($\mathbf{y} \in S$): Given: homogenized strain: ϵ; cohesive law and associated parameters and ISVs. Compute: microscale separation: $\boldsymbol{\delta}$</p> <p>Equilibrium equation: $\mathbf{t}(\mathbf{x}, \hat{\mathbf{y}}, t) - \mathbf{C}(\hat{\mathbf{y}}) : \bar{\epsilon}$ $- \int_{\Theta} \mathbf{g}(\mathbf{y}, \hat{\mathbf{y}}) : \mathbf{L} : (\mathbf{g} \odot \boldsymbol{\delta})(\mathbf{x}, \mathbf{y}, t) d\mathbf{y} = \mathbf{0}$</p> <p>Cohesive behavior: $\mathbf{t} = \hat{\mathbf{t}}(\boldsymbol{\delta}, \mathbf{q})$</p>
--	---

Figure 2: Summary of the microscale boundary value problems based on the computational homogenization approach and the eigenseparation-based approach.

multiple “potential” discontinuity paths that could form within the same microstructure.

Consider a microstructure that includes n potential discontinuity paths (or *failure paths*) as illustrated in Fig. 3. The morphology of each potential failure path is denoted as, S_a ($a = 1, \dots, n$) and assumed to be known a-priori. In the presence of multiple potential failure paths, the microscale displacement field is expressed as:

$$\mathbf{u}^1(\mathbf{x}, \mathbf{y}, t) = \mathbf{H}(\mathbf{y}) : \boldsymbol{\epsilon}^0(\mathbf{x}, t) + \sum_{a=1}^n (\mathbf{h}_a * \boldsymbol{\delta}_a)(\mathbf{x}, \mathbf{y}, t) \quad (10)$$

in which, $\mathbf{h}_a(\mathbf{y}, \hat{\mathbf{y}})$ is the separation influence function for the failure path, a ($\hat{\mathbf{y}} \in S_a$ and $\mathbf{y} \in \Theta$), and $\boldsymbol{\delta}_a(\mathbf{x}, \hat{\mathbf{y}}, t)$ denotes the separation along S_a . Following a similar algebra to that for a single failure path case, the microstructural equilibrium is expressed on each failure path as:

$$\mathbf{t}_a(\mathbf{x}, \hat{\mathbf{y}}, t) - \mathbf{C}_a(\hat{\mathbf{y}}) : \bar{\boldsymbol{\epsilon}}(\mathbf{x}, t) - \sum_{b=1}^n \int_{\Theta} \mathbf{g}_a(\mathbf{y}, \hat{\mathbf{y}}) : \mathbf{L}(\mathbf{y}) : (\mathbf{g}_b * \boldsymbol{\delta}_b)(\mathbf{x}, \mathbf{y}, t) d\mathbf{y} = \mathbf{0} \quad (11)$$

in which,

$$\mathbf{C}_a(\hat{\mathbf{y}}) := \int_{\Theta} \mathbf{g}_a(\mathbf{y}, \hat{\mathbf{y}}) : \mathbf{L}(\mathbf{y}) : \mathbf{A}(\mathbf{y}) d\mathbf{y} \quad (12)$$

Remark 1. *It is often not possible to avoid that the potential failure paths intersect each other as also illustrated in Fig. 3. At any point along the intersection of two failure paths, S_a and*

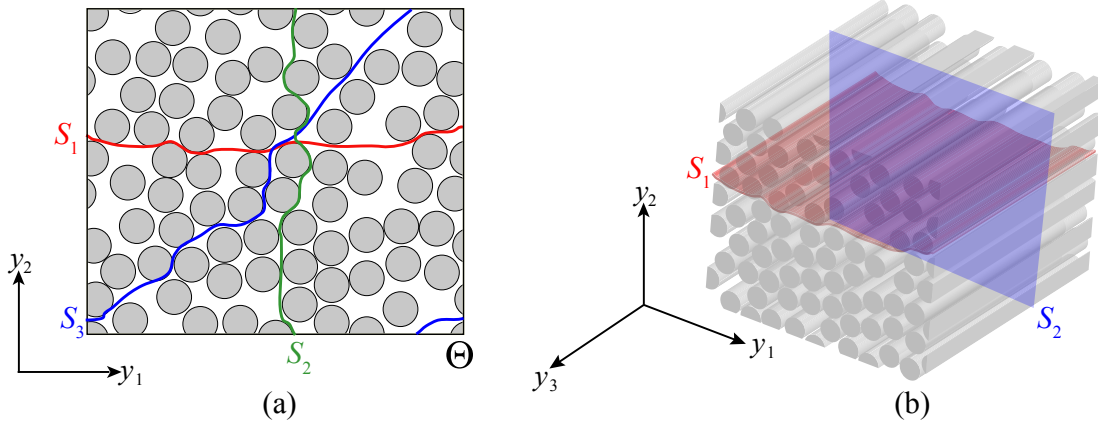


Figure 3: Schematic description of the multiple potential failure paths: (a) multiple matrix cracking modes in a 2-D microstructure volume; (b) matrix cracking (S_1) and fiber fracture modes S_2 in a 3-D microstructure volume

S_b :

$$\int_{\Theta} \mathbf{g}_a(\mathbf{y}, \hat{\mathbf{y}}) \boldsymbol{\sigma}(\mathbf{x}, \hat{\mathbf{y}}, t) d\mathbf{y} = \int_{\Theta} \mathbf{g}_b(\mathbf{y}, \hat{\mathbf{y}}) \boldsymbol{\sigma}(\mathbf{x}, \hat{\mathbf{y}}, t) d\mathbf{y}; \quad \hat{\mathbf{y}} \in (S_a \cap S_b) \subset \mathbb{R}^{n_{sd}-2} \quad (13)$$

which is clearly satisfied if the following, stronger condition holds:

$$\mathbf{g}_a(\mathbf{y}, \hat{\mathbf{y}}) = \mathbf{g}_b(\mathbf{y}, \hat{\mathbf{y}}); \quad \hat{\mathbf{y}} \in S_a \cap S_b \quad (14)$$

The condition in Eq. 14 is in fact trivial and satisfied in the formulation since the right and left hand sides of the equation both correspond to the response under the same unit separation loading.

Remark 2. In a fully random composite subjected to arbitrary loading (e.g., concrete), the orientation of the crack is primarily dictated by the loading direction on the microstructure. In such a scenario, prescribing a finite set of morphologies that a microcrack can form and propagate along may not be feasible. A dynamic failure path identification strategy could be employed instead, where a failure nucleation criterion based on a macroscopic (i.e., homogenized) or a microscopic stress, strain or energy metric dictates the nucleation state and propagation direction of the crack. Such a strategy would require the identification of the path of the microcrack and computation of the influence functions during a macroscopic analysis. In other widely applicable problems such as laminated composite structures, failure occurs due to a finite set of mechanisms (e.g., transverse matrix cracking, delamination, fiber fracture, etc.) whose orientations are dictated by the direction of the lamination. The latter set of problems is more amenable to presetting the potential failure paths, and is the focus of the current study.

2.2 Model Reduction

In what follows, we employ a reduced order approximation to obtain a small, algebraic system of equations from the eigen-separation form of the microscopic boundary value problem. For simplicity, the formulation is explained for a single failure path, but the resulting system is directly applicable to the multiple failure path case with a slightly altered interpretation, as further explained below.

We start by the approximation of the separation as a function of a number of reduced-order basis functions, $N^{(\alpha)}$:

$$\boldsymbol{\delta}(\mathbf{x}, \hat{\mathbf{y}}, t) = \sum_{\alpha=1}^m N^{(\alpha)}(\hat{\mathbf{y}}) \boldsymbol{\delta}^{(\alpha)}(\mathbf{x}, t); \quad \hat{\mathbf{y}} \in S \quad (15)$$

where, $\boldsymbol{\delta}^{(\alpha)}$ denotes the reduced-order separation coefficient associated with the α^{th} basis function, and m is the number of basis functions employed in the reduced-order approximation. The separation coefficients are taken to be microscopically nonlocal quantities, expressed as a function of nonlocal weight functions, $\nu^{(\alpha)}$ as:

$$\boldsymbol{\delta}^{(\alpha)}(\mathbf{x}, t) = \int_S \nu^{(\alpha)}(\hat{\mathbf{y}}) \boldsymbol{\delta}(\mathbf{x}, \hat{\mathbf{y}}, t) d\hat{\mathbf{y}} \quad (16)$$

Substituting Eq. 15 into Eq. 7, premultiplying the resulting equation with the weight function $\nu^{(\alpha)}$ and integrating over the domain of the failure path, S results in the following expression:

$$\mathbf{t}^{(\alpha)}(\mathbf{x}, t) - \mathbf{C}^{(\alpha)} : \bar{\boldsymbol{\epsilon}}(\mathbf{x}, t) + \sum_{\beta=1}^m \mathbf{D}^{(\alpha\beta)} \cdot \boldsymbol{\delta}^{(\beta)}(\mathbf{x}, t) = \mathbf{0}; \quad \alpha = 1, 2, \dots, m \quad (17)$$

where,

$$\mathbf{C}^{(\alpha)} := \int_S \nu^{(\alpha)}(\hat{\mathbf{y}}) \mathbf{C}(\hat{\mathbf{y}}) d\hat{\mathbf{y}} \quad (18)$$

$$\mathbf{D}^{(\alpha\beta)} := - \int_S \nu^{(\alpha)}(\hat{\mathbf{y}}) \mathbf{D}^{(\beta)}(\hat{\mathbf{y}}) d\hat{\mathbf{y}} \quad (19)$$

$$\mathbf{D}^{(\alpha)}(\hat{\mathbf{y}}) := \int_{\Theta} \mathbf{g}(\mathbf{y}, \hat{\mathbf{y}}) : \mathbf{L}(\mathbf{y}) : \mathbf{R}^{(\alpha)}(\mathbf{y}) d\mathbf{y} \quad (20)$$

$$\mathbf{R}^{(\alpha)}(\mathbf{y}) := \int_S N^{(\alpha)}(\hat{\mathbf{y}}) \mathbf{g}(\mathbf{y}, \hat{\mathbf{y}}) d\hat{\mathbf{y}} \quad (21)$$

and the traction coefficient, $\mathbf{t}^{(\alpha)}$ is defined analogous to Eq. 16.

The cohesive behavior within the failure path is interpreted as a relationship between the traction and separation coefficients instead of the point-wise quantities. In this manuscript, the

cohesive behavior within the failure path is expressed using the following traction-separation relationship:

$$\mathbf{t}^{(\alpha)} = (1 - \omega^{(\alpha)}) \mathbf{K}^{(\alpha)} \cdot \boldsymbol{\delta}^{(\alpha)} \quad (22)$$

where $\omega^{(\alpha)} \in [0, 1]$ is a scalar internal state variable that defines the progressive debonding of the cohesive surface. $\omega^{(\alpha)} = 0$ and $\omega^{(\alpha)} = 1$, respectively denote the initial state with full cohesive stiffness and a cohesionless crack along the failure path, respectively. In what follows $\omega^{(\alpha)}$ is referred to as “damage” in the failure path. $\mathbf{K}^{(\alpha)}$ is the tensor of cohesive stiffnesses, a second order tensor that is diagonal when expressed in the local basis aligned with the unit normal to the failure path, $\mathbf{n}^{(\alpha)}$:

$$\mathbf{n}^{(\alpha)} := \frac{1}{|S|} \int_S N^{(\alpha)}(\hat{\mathbf{y}}) \mathbf{n}(\hat{\mathbf{y}}) d\hat{\mathbf{y}} \quad (23)$$

Equations 17 and 22 along with the appropriate evolution equations that describe damage growth in the failure path constitute the reduced order approximation of the microscale problem in its eigenseparation form (Fig. 2). The reduced order microscale problem is an algebraic nonlinear system of equations in which, the macroscale strain acts as the forcing function and the traction and separation coefficients are evaluated as unknowns. Upon condensation (i.e., substituting Eq. 22 into Eq. 17), the number of equations in the nonlinear system is precisely $n_{\text{sd}} \times m$. The evaluation procedure for the nonlinear system is discussed in detail below. Provided that a relatively small number of shape functions are employed in the discretization of the separation fields, the evaluation of the proposed reduced order system is very efficient compared to the numerical evaluation of the microscale problem obtained from classical computational homogenization.

2.2.1 Model reduction with multiple failure paths

The reduced order representation of the microstructural equilibrium is extended to multiple failure paths in a straightforward fashion. The separation on an arbitrary failure path, a is approximated as:

$$\boldsymbol{\delta}_a(\mathbf{x}, \mathbf{y}, t) = \sum_{\alpha=1}^{m_a} N^{(a\alpha)}(\mathbf{y}) \boldsymbol{\delta}^{(a\alpha)}(\mathbf{x}, t); \quad \mathbf{y} \in S_a \quad (24)$$

The total number of basis functions used in the reduced basis approximation of all potential separation fields is denoted as $m = \sum_{a=1}^n m_a$. Using a similar algebra in the derivation of the reduced order equilibrium equation for the single failure path case, we arrive at the identical

expression of Eq. 17 if the equations are re-indexed such that:

$$\boldsymbol{\delta}^{(a\gamma)} \{a = 1 : n; \gamma = 1 : m_a\} \rightarrow \boldsymbol{\delta}^{(\alpha)} \{\alpha = 1 : m\} \quad (25)$$

$$S^{(a\gamma)} = S_a \{a = 1 : n; \gamma = 1 : m_a\} \rightarrow S^{(\alpha)} \{\alpha = 1 : m\} \quad (26)$$

Noting that $S^{(a\gamma)} = S_a$ for all $\gamma = 1, \dots, m_a$. The coefficient tensors become:

$$\mathbf{C}^{(\alpha)} := \int_{S^{(\alpha)}} \nu^{(\alpha)}(\mathbf{y}) \mathbf{C}(\mathbf{y}) d\mathbf{y} \quad (27)$$

$$\mathbf{D}^{(\alpha\beta)} := - \int_{S^{(\alpha)}} \nu^{(\alpha)}(\mathbf{y}) \mathbf{D}^{(\beta)}(\mathbf{y}) \quad (28)$$

$$\mathbf{R}^{(\alpha)}(\mathbf{y}) := \int_{S^{(\alpha)}} N^{(\alpha)}(\hat{\mathbf{y}}) \mathbf{g}(\mathbf{y}, \hat{\mathbf{y}}) d\hat{\mathbf{y}} \quad (29)$$

$$\mathbf{n}^{(\alpha)} := \frac{1}{|S^{(\alpha)}|} \int_{S^{(\alpha)}} N^{(\alpha)}(\hat{\mathbf{y}}) \mathbf{n}(\hat{\mathbf{y}}) d\hat{\mathbf{y}} \quad (30)$$

It is straightforward to compute the macroscopic stress field at an arbitrary position, $\mathbf{x} \in \Omega$ as a function of the separation coefficients. Averaging the stress field over the domain of the microstructure:

$$\bar{\boldsymbol{\sigma}}(\mathbf{x}, t) := \langle \boldsymbol{\sigma}(\mathbf{x}, \mathbf{y}, t) \rangle_{\Theta} = \bar{\mathbf{L}} : \bar{\boldsymbol{\epsilon}}(\mathbf{x}, t) + \sum_{\alpha=1}^m \mathbf{Z}^{(\alpha)} \cdot \boldsymbol{\delta}^{(\alpha)}(\mathbf{x}, t) \quad (31)$$

where,

$$\mathbf{Z}^{(\alpha)} := \langle \mathbf{L}(\mathbf{y}) : \mathbf{R}^{(\alpha)}(\mathbf{y}) \rangle_{\Theta} \quad (32)$$

$$\bar{\mathbf{L}} := \langle \mathbf{L}(\mathbf{y}) : \mathbf{A}(\mathbf{y}) \rangle_{\Theta} \quad (33)$$

in which, $\bar{\mathbf{L}}$ is the tensor of homogenized elastic moduli of the composite. The third order coefficient tensor, $\mathbf{Z}^{(\alpha)}$ provides the stress contribution due to the separation coefficient, $\boldsymbol{\delta}^{(\alpha)}$.

2.2.2 Reduced order basis and weight functions

The accuracy and computational efficiency characteristics of the D-EHM model are controlled by the order of the model (i.e., m) as well as the form of the basis and weight functions employed to discretize the separation fields. In order to ensure consistency of the formulation,

the basis and weight functions must satisfy four constraints [36]:

$$\text{Orthonormality: } \int_S \nu^{(\alpha)}(\hat{\mathbf{y}}) N^{(\beta)}(\hat{\mathbf{y}}) d\hat{\mathbf{y}} = \delta_{\alpha\beta} \quad (34a)$$

$$\text{Partition of unity: } \sum_{\alpha=1}^m N^{(\alpha)}(\hat{\mathbf{y}}) = 1; \quad \hat{\mathbf{y}} \in S \quad (34b)$$

$$\text{Positivity: } \nu^{(\alpha)}(\hat{\mathbf{y}}) \geq 0; \quad \hat{\mathbf{y}} \in S \quad (34c)$$

$$\text{Normality: } \int_S \nu^{(\alpha)}(\hat{\mathbf{y}}) d\hat{\mathbf{y}} = 1 \quad (34d)$$

in which, $\delta_{\alpha\beta}$ denotes Kronecker delta, and S is interpreted as all failure paths within the microstructure (i.e., $S = \cup_{a=1}^n S_a$). Equation 34a is a direct consequence of Eqs. 15 and 16 and implies that the weight and basis functions must exhibit orthonormality. The remainder of the constraints (i.e., Eq. 34b- 34d) respectively indicate the partition of unity of the separation fields within the microstructure; the positivity of the weight function to eliminate negative nonlocal contributions, and the weight function normalization. Derivation of these conditions have been demonstrated in Ref. [36] in the context of the EHM formulation, and is also applicable to D-EHM.

In the current manuscript, we make the simplest choice for the basis and weight functions that satisfy the four constraints mentioned above. First, each failure path within the microstructure is represented by a single basis function: $m_a = 1$ for all $a = 1, \dots, n$, hence $m = n$. Second, the basis and weight functions are taken to be piecewise constant over the failure paths:

$$N^{(\alpha)}(\hat{\mathbf{y}}) = \begin{cases} 1 & \text{if } \hat{\mathbf{y}} \in S^{(\alpha)} \\ 0 & \text{elsewhere} \end{cases} \quad \nu^{(\alpha)}(\hat{\mathbf{y}}) = \begin{cases} 1/|S^{(\alpha)}| & \text{if } \hat{\mathbf{y}} \in S^{(\alpha)} \\ 0 & \text{elsewhere} \end{cases} \quad (35)$$

Remark 3. *The reduced order modeling methodology could be enhanced in two ways. In the first approach, the number of basis functions employed to discretize each failure path could be increased (i.e., $m_a > 1$) to better represent the progressive nature of crack formation within the microstructure domain. This model improvement introduces two complications. Subdomains within the failure paths over which the piecewise constant basis functions need to be defined in a fashion that ensures model accuracy improvement compared to the present case. The presence of multiple basis functions in the same failure path also introduces a discontinuity in the separation field at the interfaces of the subdomains. In the second approach, nonlinear basis functions can be employed mimicking the ideas of the nonuniform transformation field analysis [33]. These more complex basis function selection strategies and their consequences in approximating the response fields will be the focus of future investigations. All numerical examples described in this manuscript employ Eq. 35.*

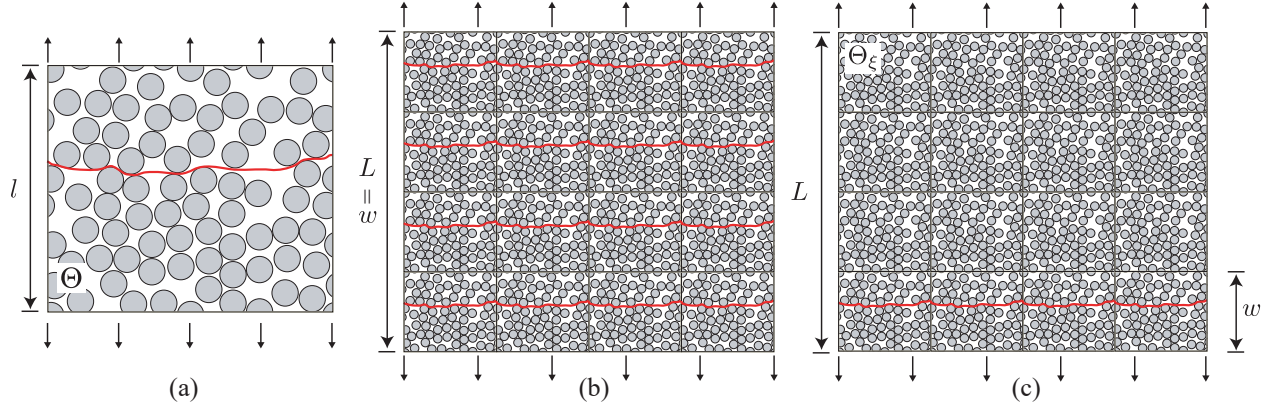


Figure 4: Schematic illustration of the scaling idea: (a) reference microstructure; (b) domain in the absence of localization represented by the repetition of the reference microstructure; (c) domain in the presence of localization, where the behavior is represented by scaling of the coefficient tensors.

2.3 Crack Localization

The macroscopic stress-strain relationship defined by the D-EHM model exhibits strain softening. If not regularized, a macroscopic analysis using the formulation above exhibits spurious mesh localization and mesh size sensitivity. In this study, we propose to regularize the formulation for mesh size sensitivity based on the idea of effective adjustment of microstructure size. The proposed idea bears resemblance to that proposed by Gitman et al. [24]. Following the crack band regularization approach of Bazant and Oh [45], damage at the macroscopic scale is allowed to localize. Mesh size consistency is achieved by adjusting the energy dissipated at the element level as a function of element size in such a way that the resulting macroscopic fracture energy is independent of the mesh size. A related concept is also used in element removal/deletion schemes with energy dissipated adjustment that are based on element sizes [46]. Unlike the crack band approach that relies on adjusting the damage evolution parameters, we adjust the size of the microstructure domain to achieve mesh size objectivity. In view of the periodicity of the microstructure, adjusting the microstructure domain in turn sets the local microcrack density and ensures energetic consistency. For computational efficiency, the size adjustment is performed in an *effective* manner by obtaining analytical equivalency relationships, rather than numerically computing a separate reduced order model for every macroscopic element with a different size.

Figure 4 schematically illustrates the proposed concept. Let L denote the size of the heterogeneous domain undergoing failure subjected to uniaxial loading. The size of the localization zone is denoted as w . Let $\xi = L/w$ denote the size scale ratio of localization. In the absence of any localization within the domain (i.e., $\xi = 1$ as shown in Fig. 4b) and in view of local periodicity, the microstructures shown in Fig. 4a and Fig. 4b behave identically and have iden-

tical microcrack densities, whereas the failure behavior in Fig. 4c is different, and has lower microcrack density.

Let $\mathfrak{R}_\xi = \mathfrak{R}(\Theta_\xi, S_\xi; \mathbf{C}, \mathbf{D}_\xi, \mathbf{Z}_\xi)$ denote the reduced order model defined by the microstructure with size scale ratio, ξ (e.g., \mathfrak{R}_1 and \mathfrak{R}_4 denote the models for Figs. 4b and 4c, respectively). The reduced order model is a function of the microstructure domain, Θ_ξ and the discontinuity paths embedded in the microstructure domain, S_ξ . For simplicity the subscript 1 is omitted from the “reference” microstructure (i.e., $\mathfrak{R} = \mathfrak{R}_1$). We seek to find an equivalent representation of the ROM with an arbitrary size scale ratio as a function of the reference ROM. Let:

$$\hat{\mathfrak{R}}_\xi = \mathfrak{R}(\Theta, S; \mathbf{C}, \eta(\xi)\mathbf{D}, \eta(\xi)\mathbf{Z}) = \mathfrak{R}_\xi = \mathfrak{R}(\Theta_\xi, S_\xi; \mathbf{C}, \mathbf{D}_\xi, \mathbf{Z}_\xi) \quad (36)$$

The equivalency is achieved by scaling the coefficient tensors (\mathbf{D} and \mathbf{Z}) associated with the reference microstructure using a function η expressed in terms of the size scale ratio. In the numerical simulations, the size of the localization zone is dictated by the size of the macroscale element. We therefore express the size scale ratio as $\xi = l/h$, where l and h respectively denote the size of the microstructure and the macroscopic element length.

By this approach, for each element of the macroscale discretization, we employ the regularized ROM, $\hat{\mathfrak{R}}_{l/h}$. The above discussion therefore indicates that the size of the microstructure volume, and hence microcrack density within the element, is effectively adjusted as a function of macroscale element size to ensure mesh size objectivity. The implementation of this approach is computationally efficient provided that closed form expression for coefficient tensor scaling (i.e., $\eta(\xi)$) is available. In what follows, we demonstrate the derivation of η under simplified conditions. The detailed derivation of coefficient tensor scaling for the more general case is provided in the Appendix.

Consider a microstructure with one failure path subjected to failure under mode I condition, such that the separation coefficients are expressed of the form, $\boldsymbol{\delta} = \delta_N \mathbf{n}$. Since only one failure path is considered, we omit the use of superscript (1) for simplicity of the presentation. We make the approximation that the Mode I condition is achieved by considering the macroscale strain state of the form: $\bar{\boldsymbol{\epsilon}} = \hat{\epsilon}_N \mathbf{n} \otimes \mathbf{n}$. In fact, exact derivation of pure Mode I condition requires considering nonzero normal strains along the two orthogonal directions as shown in Eq. A1, but the approximation provided by a pure uniaxial strain state turns out to be sufficiently accurate. We further consider a traction-separation law such that the softening behavior exhibits constant softening slope, resulting in a homogenized stress-strain behavior that also softens with a constant slope. The microscale equilibrium using the regularized ROM, $\hat{\mathfrak{R}}_\xi$ is expressed as:

$$[(1 - \omega) \mathbf{K} + \eta(\xi)\mathbf{D}] \cdot \boldsymbol{\delta} - \mathbf{C} : \bar{\boldsymbol{\epsilon}} = 0 \quad (37)$$

Substituting the forms of the separation and the macroscopic strain tensors into Eq. 37,

taking an inner product of the resulting equation with \mathbf{n} yields the following scalar equation:

$$[(1 - \omega) K + \eta(\xi)D] \delta_N - C\hat{\epsilon}_N = 0 \quad (38)$$

where, $K = \mathbf{n} \cdot \mathbf{K} \cdot \mathbf{n}$, $D = \mathbf{n} \cdot \mathbf{D} \cdot \mathbf{n}$ and $C = \mathbf{n} \cdot \mathbf{C} : (\mathbf{n} \otimes \mathbf{n})$.

Similarly, the macroscopic stress-strain relationship is:

$$\bar{\boldsymbol{\sigma}} = \bar{\mathbf{L}} : \bar{\boldsymbol{\epsilon}} + \eta(\xi)\mathbf{Z} \cdot \boldsymbol{\delta} \quad (39)$$

Substituting the forms of the separation and macroscopic strain tensors into the above equation and considering the component of the stress field along the normal direction results in:

$$\bar{\sigma} = \bar{E}\hat{\epsilon}_N + \eta(\xi)Z\delta_N \quad (40)$$

in which, $\bar{\sigma} = \mathbf{n} \cdot \bar{\boldsymbol{\sigma}} \cdot \mathbf{n}$, $\bar{E} = (\mathbf{n} \otimes \mathbf{n}) : \bar{\mathbf{L}} : (\mathbf{n} \otimes \mathbf{n})$, and $Z = (\mathbf{n} \otimes \mathbf{n}) : \mathbf{Z} \cdot \mathbf{n}$. Differentiating Eq. 40 with respect to the macroscopic strain and considering linear softening, the softening slope of the stress-strain curve is expressed as:

$$E_\xi^s = \bar{E} + \frac{\eta(\xi)ZC}{A + \eta(\xi)D} \quad (41)$$

where, A is the softening slope of the traction-separation relationship. A straightforward analysis of the heterogeneous domains shown in Fig. 4b and 4c under simplifying one dimensional conditions indicate that the softening slope of a domain localizing with a scaling ratio of ξ is:

$$E_\xi^s = \frac{\bar{E}E^s}{\xi\bar{E} + (1 - \xi)E^s} \quad (42)$$

in which, E^s denotes the softening slope of the reference microstructure (i.e., when $\mathfrak{R} = \mathfrak{R}_1$). Noting that $\eta(1) = 1$ (i.e., $\mathfrak{R}_1 = \hat{\mathfrak{R}}_1$) and substituting Eq. 41 into Eq. 42, a closed form expression for the scaling relationship is obtained:

$$\eta(\xi) = \frac{\xi A}{A + (1 - \xi)(D\bar{E} + ZC)\bar{E}^{-1}} \quad (43)$$

For a given macroscopic element size, h , the scaled coefficient tensors are employed in the reduced order model. The expressions for the coefficient tensor scaling in the presence of multiple modes of loading and failure paths are more complicated since scaling for each failure path and mode is different. Details of the scaling laws in the general case are provided in the Appendix. The scaled coefficient tensor, $\hat{\mathbf{D}}^{(\alpha\beta)}$ takes the form:

$$\hat{\mathbf{D}}^{(\alpha\beta)} \left(\xi^{(\alpha)} \right) = \boldsymbol{\eta}^{(\alpha)} \left(\xi^{(\alpha)} \right) \cdot \mathbf{D}^{(\alpha\beta)} \quad (44)$$

When expressed in terms of the local coordinate systems aligned with the unit normals of the failure paths, the matrix form of the scaling tensor is diagonal:

$$\left[\boldsymbol{\eta}^{(\alpha)} \left(\xi^{(\alpha)} \right) \right] = \begin{bmatrix} \eta_N^{(\alpha)}(\xi^{(\alpha)}) & 0 & 0 \\ 0 & \eta_{S_1}^{(\alpha)}(\xi^{(\alpha)}) & 0 \\ 0 & 0 & \eta_{S_2}^{(\alpha)}(\xi^{(\alpha)}) \end{bmatrix} \quad (45)$$

in which, $\xi^{(\alpha)}$ denotes the size scale ratio for the failure path α . The size scale ratio for a failure path loaded in normal and shear modes is taken to be the same. Each component of the scaling parameter is of the same form as in Eq. 43, but computed in terms of the appropriate coefficient and the scaling parameter as described in the Appendix.

$\hat{\mathbf{Z}}^{(\alpha)}(\xi^{(\alpha)})$ is a third order tensor and its scaling takes a slightly different form, but expressed in terms of the same scaling parameters. Expressing in the matrix form:

$$\left[\hat{\mathbf{Z}}^{(\alpha)} \left(\xi^{(\alpha)} \right) \right] = \begin{bmatrix} \eta_N^{(\alpha)} \mathbf{Z}_{11}^{(\alpha)} & \eta_{S_1}^{(\alpha)} \mathbf{Z}_{12}^{(\alpha)} & \eta_{S_2}^{(\alpha)} \mathbf{Z}_{13}^{(\alpha)} \\ \eta_{S_1}^{(\alpha)} \mathbf{Z}_{12}^{(\alpha)} & \mathbf{Z}_{22}^{(\alpha)} & \mathbf{Z}_{23}^{(\alpha)} \\ \eta_{S_2}^{(\alpha)} \mathbf{Z}_{13}^{(\alpha)} & \mathbf{Z}_{23}^{(\alpha)} & \mathbf{Z}_{33}^{(\alpha)} \end{bmatrix} \quad (46)$$

where the third component of $\mathbf{Z}^{(\alpha)}$ is suppressed for brevity (i.e., $\mathbf{Z}_{ij}^{(\alpha)} \leftarrow Z_{ijp}^{(\alpha)}$ in the indicial form).

Remark 4. *The scaling law formulated above makes use of characteristic lengths of the macroscopic element to determine $\xi^{(\alpha)}$. Algorithms for identifying the element lengths relative to the crack orientation have been proposed and studied previously (see e.g., [47, 48]) for the crack band method. In the verification studies below, we employed structured and crack aligned meshes within critical regions of the macrostructure. For a given failure path, the characteristic length for normal and shear modes are taken to be the length of the macroscopic element along the failure path normal.*

2.4 Residual stiffness correction

Eigenstrain-based homogenization models have been shown to exhibit spurious post-failure residual stiffness, particularly when low order models are employed [36]. The existence of non-trivial residual stiffness allows the macroscopic element to retain some load carrying capacity after failure and alters load redistribution in a failure propagation scenario. This problem has been tied to the incompatibility of eigenstrains by Furuhashi and Mura [49] and a number of solution strategies have been discussed in Refs. [34, 36, 50]. We encountered this problem in the current formulation as well. In the current manuscript, the issue of post-failure residual stiffness is alleviated by extending the idea of coefficient tensor scaling.

Herein, we demonstrate the proposed scaling approach for the simple case shown in Fig. 4. Consider the following scaled reduced order model:

$$\hat{\mathfrak{R}}_\xi^r = \mathfrak{R}(\Theta, S; \mathbf{C}, \tilde{\eta}(\xi)\mathbf{D}, \tilde{\eta}(\xi)\eta^r\mathbf{Z}) \quad (47)$$

where, $\tilde{\eta}(\xi)$ and η^r stand for the scaling parameters for crack localization and residual stiffness correction, respectively. The residual stiffness correction only affects the macroscopic stress-strain relationship through scaling of \mathbf{Z} . Considering mode I loading of the failure path, the scalar microstructure equilibrium equation and the macroscopic stress-strain relationship becomes:

$$[(1 - \omega)K + \tilde{\eta}(\xi)D] \delta_N - C\hat{\epsilon}_N = 0 \quad (48)$$

$$\bar{\sigma} = \bar{E}\hat{\epsilon}_N + \tilde{\eta}(\xi)\eta^r Z\delta_N \quad (49)$$

Following a similar derivation as in the previous section, the softening slope of macroscopic stress-strain curve is expressed in terms of the two scaling factors $\tilde{\eta}$ and η^r :

$$E_\xi^s = \bar{E} + \frac{\tilde{\eta}(\xi)\eta^r ZC}{A + \tilde{\eta}(\xi)D} \quad (50)$$

Considering the reference microstructure (i.e., $\xi = 1$) and after damage along the failure path reaches unity, the slope of the traction-separation curve vanishes ($A = 0$). The scaled residual stiffness is then:

$$\hat{E}^r(\eta^r) = \bar{E} + \eta^r \frac{ZC}{D} \quad (51)$$

In the absence of correction, the residual stiffness predicted by the model is $E^r = \hat{E}^r(\eta^r = 1)$. We therefore seek to set η^r such that the resulting residual stiffness is sufficiently small. Defining a correction factor $k^r = \hat{E}^r/E^r$, the scaling factor is obtained from Eq. A30 as:

$$\eta^r = -(1 - k^r) \frac{D\bar{E}}{ZC} + k^r \quad (52)$$

Noting that the residual stiffness scaling is independent of the length scale ratio, ξ and by substituting Eqs. 50 and 52 into Eq. 42, the expression for the scaling parameter of crack localization is obtained:

$$\tilde{\eta} = \frac{\xi A}{A + k^r(1 - \xi)(D\bar{E} + ZC)\bar{E}^{-1}} \quad (53)$$

Equation 53 differs from Eq. 43 only by the presence of the correction factor k^r . If the uncorrected residual stiffness predicted by the reduced order model is zero, the second term in the denominator of Eq. 53 vanishes and the scaling parameter is $\tilde{\eta} = \xi$, which is the classical scaling law for the crack band model. Similarly, setting the residual correction factor, k^r to a

Reduced Order Model:

Given: homogenized strain: $\bar{\epsilon}$; scaled coefficient tensors: $\bar{\mathbf{L}}$, $\mathbf{C}^{(\alpha)}$, $\hat{\mathbf{D}}^{(\alpha\beta)}$ and $\hat{\mathbf{Z}}^{(\alpha\beta)}$;
constituent material parameters for cohesive behavior

Compute: homogenized stress: $\bar{\sigma}$

Equilibrium equation: $\mathbf{t}^{(\alpha)}(\mathbf{x}, t) - \mathbf{C}^{(\alpha)} : \bar{\epsilon}(\mathbf{x}, t) + \sum_{\beta=1}^m \hat{\mathbf{D}}^{(\alpha\beta)} \cdot \boldsymbol{\delta}^{(\beta)}(\mathbf{x}, t) = \mathbf{0}; \quad \alpha = 1, 2, \dots, m$

Cohesive law: $\mathbf{t}^{(\alpha)}(\mathbf{x}, t) = \left(1 - \omega^{(\alpha)}(\mathbf{x}, t)\right) \mathbf{K}^{(\alpha)} \cdot \boldsymbol{\delta}^{(\alpha)}(\mathbf{x}, t)$

Damage evolution equations: $\dot{\omega}^{(\alpha)} = f(\boldsymbol{\delta}^{(\alpha)}, \mathbf{q}^{(\alpha)})$

Homogenized stress update: $\bar{\sigma}(\mathbf{x}, t) = \bar{\mathbf{L}} : \bar{\epsilon}(\mathbf{x}, t) + \sum_{\alpha=1}^m \hat{\mathbf{Z}}^{(\alpha)} \cdot \boldsymbol{\delta}^{(\alpha)}(\mathbf{x}, t)$

Figure 5: Summary of the reduced order microscale problem.

very small value recovers the simple relationship: $\tilde{\eta} \approx \xi$.

Employing both the residual stiffness correction and scaling for localization in the general case of failure paths and multiple modes of loading, the matrix form of the localization tensor for scaling $\hat{\mathbf{D}}^{(\alpha\beta)}$ becomes (considering sufficiently small residual stiffness correction):

$$\left[\tilde{\boldsymbol{\eta}}^{(\alpha)}(\xi^{(\alpha)}) \right] = \xi^{(\alpha)} \begin{bmatrix} 1 & 0 & 0 \\ 0 & 1 & 0 \\ 0 & 0 & 1 \end{bmatrix} \quad (54)$$

The form for scaling of $\hat{\mathbf{Z}}^{(\alpha)}(\xi^{(\alpha)})$ is the same as in Eq. 46, but includes the residual correction terms. In the matrix form defined based on the local basis aligned with the failure path normals, we obtain:

$$\left[\hat{\mathbf{Z}}^{(\alpha)}(\xi^{(\alpha)}) \right] = \begin{bmatrix} \xi^{(\alpha)} \eta_N^{r(\alpha)} \mathbf{Z}_{11}^{(\alpha)} & \xi^{(\alpha)} \eta_{S_1}^{r(\alpha)} \mathbf{Z}_{12}^{(\alpha)} & \xi^{(\alpha)} \eta_{S_2}^{r(\alpha)} \mathbf{Z}_{13}^{(\alpha)} \\ \xi^{(\alpha)} \eta_{S_1}^{r(\alpha)} \mathbf{Z}_{12}^{(\alpha)} & \mathbf{Z}_{22}^{(\alpha)} & \mathbf{Z}_{23}^{(\alpha)} \\ \xi^{(\alpha)} \eta_{S_2}^{r(\alpha)} \mathbf{Z}_{13}^{(\alpha)} & \mathbf{Z}_{23}^{(\alpha)} & \mathbf{Z}_{33}^{(\alpha)} \end{bmatrix} \quad (55)$$

in which, the values of $\eta_N^{r(\alpha)}$, $\eta_{S_1}^{r(\alpha)}$ and $\eta_{S_2}^{r(\alpha)}$ are obtained analogously to the 1-D loading case described above. The detailed expressions of these factors are provided in the Appendix.

Figure 5 shows the summary of the governing equations of the resulting reduced order system, which is evaluated for the homogenized stress.

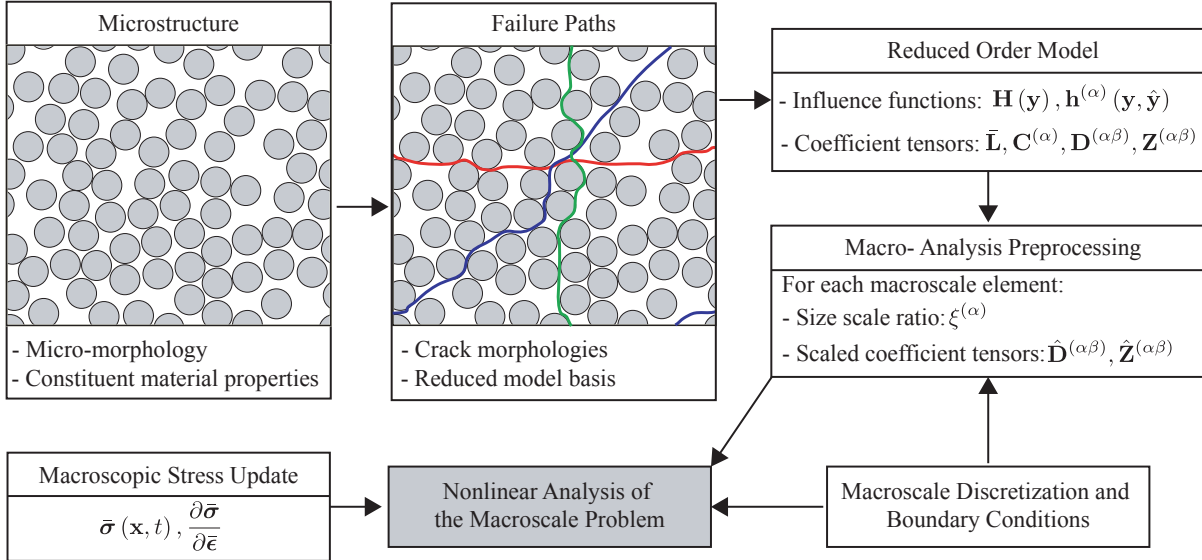


Figure 6: Numerical implementation strategy.

3 Numerical Implementation

The overall strategy for the numerical implementation of the D-EHM model is shown in Fig. 6. The implementation consists of the construction of the reduced order microstructure model at the *pre-processing* stage, and the evaluation of the macroscopic problem.

The pre-processing stage consists of the following steps: (1) Characterization and discretization of the material microstructure; (2) Identification of crack morphologies to be included in the reduced order model; (3) Evaluation of microstructure problems to compute the influence functions, and numerical integrations to compute the coefficient tensors; (4) Identification of the size scale ratios and scaling the coefficient tensors for mesh size and residual stiffness. In the current manuscript, simple unit cell morphologies (i.e., square and hexagonal) have been employed. In general, it is also possible to consider representative (i.e., prior to fracture) microstructures with randomly distributed fibers generated using appropriate statistical metrics. The crack morphologies to be included in the reduced order model could be identified based on (a) a-priori selection of failure paths for specific microstructure/loading conditions the macroscopic structure is expected to undergo; and (b) dynamic identification of the failure path during the macroscopic analysis, where the failure path is included in the reduced order model once a critical state of damage onset is detected. This study focused on the former strategy, where the number and morphologies of the failure paths are selected based on set of expected failure modes (e.g., transverse matrix crack, fiber fracture). The role of the selection of microstructure and failure path morphology is investigated in Section 4.1.3. The evaluation of the elastic and separation influence functions follow the procedures outlined in Ref. [35] and

skipped herein for brevity. The computation of the size scale ratios require the identification of the characteristic element lengths associated with each failure path at each macroscale element. The average length of the macroscale element along the direction of the failure path normal, $\mathbf{n}^{(\alpha)}$ is used.

The macroscale problem is evaluated using the commercial finite element analysis package, Abaqus. The reduced microstructure model summarized in Fig. 5 constitutes the homogenized stress update at a quadrature point, and incorporated into Abaqus using the user supplied subroutine capability, UMAT. Identification of size scale ratios and scaling of the coefficient tensors are performed immediately before the macro-analysis, using the user supplied subroutine, UEXTERNDB.

The use of standard finite element method to evaluate the macroscale problem limits the general applicability of the approach, particularly when cracks arbitrarily cross the macroscale elements. This issue is similar to the difficulties encountered in the classical crack band approach [48]. In the context of long fiber reinforced composite problems, this issue is typically circumvented by aligning the mesh with the fiber orientation, which allows the dominant failure modes to align with the mesh [51, 52]. The extension of the proposed multiscale approach to arbitrary crack orientations with respect to the mesh requires enrichment of the standard approximation basis at the macroscale (e.g., using XFEM or other strong discontinuity methods), local mesh realignment, or other advanced methods. The numerical examples discussed below employ fiber aligned macroscale meshes.

3.1 Damage evolution equations

Damage evolution is expressed as a monotonically increasing function of the history variable, $\kappa^{(\beta)}$ as:

$$\omega^{(\beta)} = \Phi \left(\kappa^{(\beta)} \right) \quad (56)$$

where,

$$\kappa^{(\beta)} = \max_{\tau \in [0, t]} \left\{ \left\langle \nu^{(\beta)}(\tau) - \nu_0^{(\beta)} \right\rangle_+ \right\} \quad (57)$$

in which, $\nu^{(\beta)}(\tau)$ and $\nu_0^{(\beta)}$ are the damage equivalent separation and the initial damage equivalent separation, respectively. $\nu_0^{(\beta)}$ is a parameter that indicates damage initiation (i.e., the value of $\nu^{(\beta)}(\tau)$ below which damage does not evolve). $\langle \cdot \rangle_+$ represents the Macaulay bracket expressed as $\langle \cdot \rangle_+ = [(\cdot) + |\cdot|]/2$. Damage equivalent separation can be expressed as a function of the components of the separation coefficients:

$$\nu^{(\beta)} = k_N^{(\beta)} \hat{\delta}_N^{(\beta)} + k_S^{(\beta)} \sqrt{\left(\hat{\delta}_{S_1}^{(\beta)} \right)^2 + \left(\hat{\delta}_{S_2}^{(\beta)} \right)^2} \quad (58)$$

in which, $[\hat{\boldsymbol{\delta}}^{(\beta)}] = [\hat{\delta}_N^{(\beta)}, \hat{\delta}_{S_1}^{(\beta)}, \hat{\delta}_{S_2}^{(\beta)}]$ is the separation vector and its components expressed along the basis aligned with the failure path normal (i.e., $\hat{\delta}_N^{(\beta)}$ is normal separation and $\hat{\delta}_{S_i}^{(\beta)}$, $i = 1, 2$ are tangential separation components). Expressed in terms of the same basis, the tensor of cohesive stiffnesses become:

$$[\mathbf{K}^{(\beta)}] = \begin{bmatrix} k_N^{(\beta)} & 0 & 0 \\ 0 & k_S^{(\beta)} & 0 \\ 0 & 0 & k_S^{(\beta)} \end{bmatrix} \quad (59)$$

k_N and k_S are the normal and tangential stiffnesses, respectively.

The damage evolution in the failure path as a function of the history variable has the form:

$$\Phi(\kappa^{(\beta)}) = \begin{cases} \frac{1}{\alpha_2^{(\beta)}} \arctan(\alpha_1^{(\beta)} \kappa^{(\beta)}) & \text{if } \kappa^{(\beta)} \leq \frac{\tan(\alpha_2^{(\beta)})}{\alpha_1^{(\beta)}} \\ 1 & \text{otherwise} \end{cases} \quad (60)$$

In the numerical implementation, the presence of Macaulay bracket in Eq. 57 introduces a discontinuity and results in lack of convergence in some cases. In order to improve convergence of the nonlinear evaluation of the system, we replace the Macaulay bracket with a C^1 continuous approximation, which introduces continuity by the addition of a small arc with radius r at the elbow of the ramp (i.e., Macaulay) function (see Ref. [53]):

$$\langle x \rangle_c = \begin{cases} 0 & x < -\tan^{-1}(3\pi r/8) \\ r - \sqrt{r^2 - [x + \tan^{-1}(3\pi r/8)]^2} & -\tan^{-1}(3\pi r/8) \leq x \leq \frac{\tan^{-1}(3\pi r/8)}{\sqrt{2}} \\ x & x > \frac{\tan^{-1}(3\pi r/8)}{\sqrt{2}} \end{cases} \quad (61)$$

In the following numerical examples, r is selected to be 8.5×10^{-4} .

3.2 Macroscopic stress update procedure

Given: Homogenized strain ${}_t\bar{\boldsymbol{\epsilon}}$ and its increment $\Delta\bar{\boldsymbol{\epsilon}}$, separations in local coordinate system ${}_t\hat{\boldsymbol{\delta}}^{(\beta)}$ and damage variables ${}_t\omega^{(\beta)}$ of each failure path ($\beta = 1, 2, \dots, m$). The left subscript denotes the incremental step, i.e., ${}_t(\cdot)$ and ${}_{t+\Delta t}(\cdot)$ stands for the variables at the previous and current increments, respectively. For simplicity, subscript ${}_{t+\Delta t}(\cdot)$ is omitted for simplicity.

Compute: The macroscopic stress $\bar{\boldsymbol{\sigma}}$; current separations $\hat{\boldsymbol{\delta}}^{(\beta)}$ and damage variables $\omega^{(\beta)}$ of each failure path.

In this section, the coefficient tensors and other tensors are expressed in matrix form following the Voigt notation. To obtain the separation vector $\hat{\boldsymbol{\delta}}^{(\beta)} = [\hat{\delta}_N^{(\beta)}, \hat{\delta}_{S_1}^{(\beta)}, \hat{\delta}_{S_2}^{(\beta)}]$, the governing equations of the reduced order model (Fig. 5) are solved using the Newton-Raphson

method. A penalty term is added to enforce contact constraint along the failure paths under compression. The general form of the resulting nonlinear system is given as:

$$\Psi = \mathbf{M}(\mathbf{d})\mathbf{d} + \mathbf{f}(\bar{\boldsymbol{\epsilon}}) + \mathbf{f}^c(\mathbf{d}) = \mathbf{0} \quad (62)$$

where \mathbf{f} is the force vector, \mathbf{f}^c is the penalty function, \mathbf{d} is the state variable vector constituted by the separation vectors: $\mathbf{d} = [\hat{\boldsymbol{\delta}}^{(1)}, \hat{\boldsymbol{\delta}}^{(2)}, \dots, \hat{\boldsymbol{\delta}}^{(m)}]^T$. Based on Eq. 17, \mathbf{M} is defined as:

$$\mathbf{M} = \begin{bmatrix} (1 - \omega^{(1)})\mathbf{K}^{(1)} + \mathbf{D}^{(11)} & \mathbf{D}^{(12)} & \dots & \mathbf{D}^{(1m)} \\ \mathbf{D}^{(21)} & (1 - \omega^{(2)})\mathbf{K}^{(2)} + \mathbf{D}^{(22)} & \dots & \mathbf{D}^{(2m)} \\ \vdots & \vdots & \ddots & \vdots \\ \mathbf{D}^{(m1)} & \mathbf{D}^{(m2)} & \dots & (1 - \omega^{(m)})\mathbf{K}^{(m)} + \mathbf{D}^{(mm)} \end{bmatrix} \quad (63)$$

where $\mathbf{K}^{(\beta)}$ represents cohesive stiffnesses and the matrix form of the coefficient tensor is stated as $\mathbf{D}^{(\alpha\beta)} = [D_{ij}^{(\alpha\beta)}]$; $i, j = 1, 2, 3$. The damage variable $\omega^{(\beta)}$ is computed using the damage evolution equations (Section 3.1) in terms of the corresponding separation $\hat{\boldsymbol{\delta}}^{(\beta)}$.

The force vector, $\mathbf{f}(\bar{\boldsymbol{\epsilon}})$ is given as:

$$\mathbf{f} = [\mathbf{C}^{(1)}; \mathbf{C}^{(2)}; \dots; \mathbf{C}^{(m)}]\bar{\boldsymbol{\epsilon}} \quad (64)$$

in which, semicolon indicates column matrix construction, and the components of the homogenized strain vector is expressed in the Voigt form: $\bar{\boldsymbol{\epsilon}} = [\hat{\epsilon}_{11}, \hat{\epsilon}_{22}, \hat{\epsilon}_{33}, \hat{\epsilon}_{12}, \hat{\epsilon}_{13}, \hat{\epsilon}_{23}]^T$.

The penalty function $\mathbf{f}^c(\mathbf{d})$ to enforce the unilateral contact constraint is given as:

$$\mathbf{f}^c = \frac{1}{\chi} [\langle \delta_N^{(1)} \rangle_-, 0, 0, \langle \delta_N^{(2)} \rangle_-, 0, 0, \dots, \langle \delta_N^{(m)} \rangle_-, 0, 0]^T \quad (65)$$

where $\chi \ll 1$ is the penalty parameter, and $\langle \cdot \rangle_-$ is defined as $\langle \cdot \rangle_- = [|\cdot| - (\cdot)]/2$.

Based on the definitions above, the solution procedure for the nonlinear system consists of the following steps:

1. Update the homogenized strain: $\bar{\boldsymbol{\epsilon}} = {}_t\bar{\boldsymbol{\epsilon}} + \Delta\bar{\boldsymbol{\epsilon}}$;
2. Initialize the unknown coefficients: ${}^0\mathbf{d} = {}_t\mathbf{d}$;
3. Loop until convergence;
 - 3a. Compute the system residual: ${}^k\partial\Psi({}^k\mathbf{d})$;
 - 3b. Check convergence: $\|{}^k\partial\Psi\| \leq tol$;
 - 3c. If convergence: Exit loop;
 - 3d. Compute system Jacobian: ${}^k(\partial\Psi/\partial\mathbf{d})$;
 - 3e. Update unknown coefficients: ${}^{k+1}\mathbf{d} = {}^k\mathbf{d} - {}^k(\partial\Psi/\partial\mathbf{d})^{-1}{}^k\partial\Psi$;
 - 3f. $k \leftarrow k + 1$

4. Update the macroscopic stress $\bar{\boldsymbol{\sigma}}$ based on Eq. 31.

3.3 Macroscopic tangent moduli

A closed form expression for the macroscopic tangent moduli tensor is defined based on Eq. 31:

$$\mathcal{L} = \frac{\partial \bar{\boldsymbol{\sigma}}}{\partial \bar{\boldsymbol{\epsilon}}} = \bar{\mathbf{L}} + \sum_{\beta=1}^m \mathbf{Z}^{(\beta)} \frac{\partial \hat{\boldsymbol{\delta}}^{(\beta)}}{\partial \bar{\boldsymbol{\epsilon}}} \quad (66)$$

The derivative of the separation vector with respect to the homogenized strain is computed by leveraging Eq. 62 and expressing the residual as $(\mathbf{d}(\bar{\boldsymbol{\epsilon}}), \bar{\boldsymbol{\epsilon}})$:

$$\frac{\partial \mathbf{d}}{\partial \bar{\boldsymbol{\epsilon}}} = - \left[\frac{\partial \Psi}{\partial \mathbf{d}} \right]^{-1} \frac{\partial \Psi}{\partial \bar{\boldsymbol{\epsilon}}} \quad (67)$$

where,

$$\frac{\partial \Psi}{\partial \bar{\boldsymbol{\epsilon}}} = [\mathbf{C}^{(1)}; \mathbf{C}^{(2)}; \dots; \mathbf{C}^{(m)}] \quad (68)$$

and

$$\frac{\partial \Psi}{\partial \mathbf{d}} = \frac{\partial \mathbf{M}}{\partial \mathbf{d}} \mathbf{d} + \mathbf{M} + \frac{\partial \mathbf{f}^c}{\partial \mathbf{d}} \quad (69)$$

The derivative of penalty function is given as:

$$\frac{\partial \mathbf{f}^c}{\partial \mathbf{d}} = \frac{1}{2\chi} \begin{bmatrix} \mathbf{F}_c^{(1)} & \mathbf{0} & \dots & \mathbf{0} \\ \mathbf{0} & \mathbf{F}_c^{(2)} & \dots & \mathbf{0} \\ \vdots & \vdots & \ddots & \vdots \\ \mathbf{0} & \mathbf{0} & \dots & \mathbf{F}_c^{(m)} \end{bmatrix}; \quad \mathbf{F}_c^{(\beta)} = \begin{bmatrix} 1 - \text{sgn}(\hat{\delta}_N^{(\beta)}) & 0 & 0 \\ 0 & 0 & 0 \\ 0 & 0 & 0 \end{bmatrix} \quad (70)$$

The derivative of \mathbf{M} is calculated by:

$$\frac{\partial \mathbf{M}}{\partial \mathbf{d}} = \sum_{\beta=1}^m \frac{\partial \mathbf{M}}{\partial \omega^{(\beta)}} \frac{\partial \omega^{(\beta)}}{\partial \mathbf{d}} \quad (71)$$

in which the only nonzero components are $-\mathbf{K}^{(\beta)}$ and $\partial \omega^{(\beta)} / \partial \hat{\boldsymbol{\delta}}^{(\beta)}$, respectively. The derivative of damage $\omega^{(\beta)}$ can be expanded through the damage evolution equations by the chain rule:

$$\frac{\partial \omega^{(\beta)}}{\partial \hat{\boldsymbol{\delta}}^{(\beta)}} = \frac{\partial \omega^{(\beta)}}{\partial \kappa^{(\beta)}} \frac{\partial \kappa^{(\beta)}}{\partial \nu^{(\beta)}} \frac{\partial \nu^{(\beta)}}{\partial \hat{\boldsymbol{\delta}}^{(\beta)}} = \frac{\alpha_1 H_c(\Delta \nu^{(\beta)})}{\alpha_2 [1 + (\alpha_1 \kappa^{(\beta)})^2]} \left[k_N^{(\beta)}, k_S^{(\beta)} \frac{\hat{\delta}_{S_1}^{(\beta)}}{\|\hat{\boldsymbol{\delta}}_S^{(\beta)}\|}, k_S^{(\beta)} \frac{\hat{\delta}_{S_2}^{(\beta)}}{\|\hat{\boldsymbol{\delta}}_S^{(\beta)}\|} \right]^T$$

where $\Delta \nu^{(\beta)}$ stands for the increment of equivalent separation $k \nu^{(\beta)} - \iota \nu^{(\beta)}$, $\|\hat{\boldsymbol{\delta}}_S^{(\beta)}\| = \sqrt{(\hat{\delta}_{S_1}^{(\beta)})^2 + (\hat{\delta}_{S_2}^{(\beta)})^2}$,

the function H_c is the derivative of the modified Macaulay bracket in Eq. 61:

$$H_c(x) = \begin{cases} 0 & x < -\tan^{-1}(3\pi r/8) \\ \frac{x + \tan^{-1}(3\pi r/8)}{\sqrt{r^2 - [x + \tan^{-1}(3\pi r/8)]^2}} & -\tan^{-1}(3\pi r/8) \leq x \leq \frac{\tan^{-1}(3\pi r/8)}{\sqrt{2}} \\ 1 & x > \frac{\tan^{-1}(3\pi r/8)}{\sqrt{2}} \end{cases} \quad (72)$$

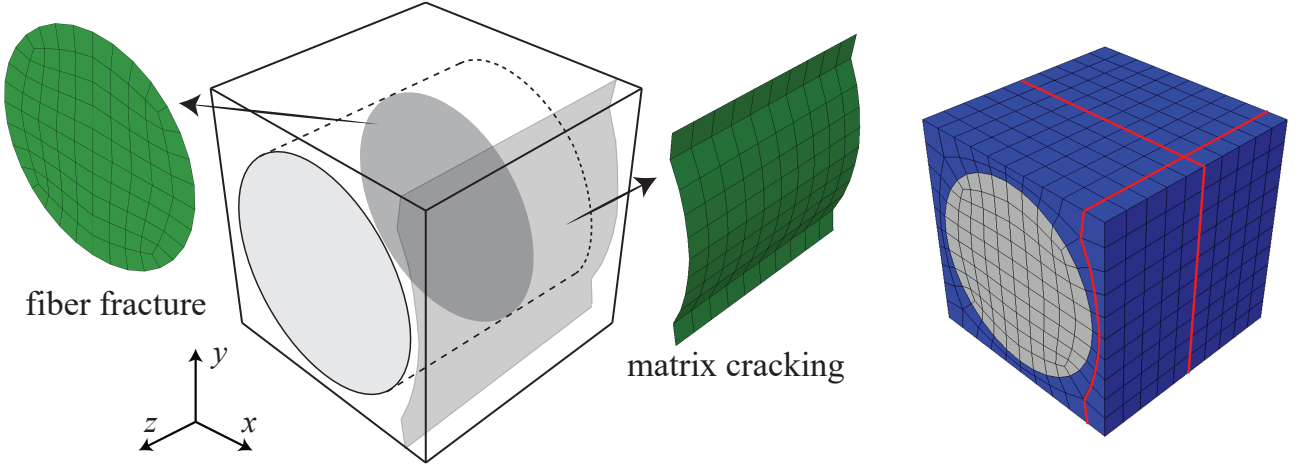


Figure 7: Microstructure configuration with failure paths of “transversely matrix cracking” and “fiber fracture”.

4 Numerical Verification

4.1 Unnotched lamina analyses

The performance of D-EHM model is first assessed in the context of uniformly loaded specimens, which corresponds to the behavior of an unnotched lamina. Figure 7 shows the microstructural configuration and the failure paths employed in the analysis. The unit cell is a unidirectional fiber-reinforced matrix with 65% fiber volume fraction. Two failure paths are considered ($m = 2$). The “transverse matrix cracking” path resides within the domain of the matrix material, whereas the fiber fracture path is within the domain of the fiber material. The matrix cracking and fiber fracture paths are approximate planes with normals along x and z directions, respectively as indicated in Fig. 7. These two failure paths correspond to two of the primary failure modes observed in laminated fiber reinforced composites subjected to tension loading. In case of failure under uni-axial loading along the z direction, the unit cell is expected to undergo failure by fiber fracture as well as the fracture within the matrix ligament. Under this loading condition, the matrix ligament failure is expected to immediately

follow or simultaneously occur with fiber fracture. In the current model, the fracture of the matrix ligament is ignored in view of the high disparity between the fiber and matrix moduli, and due to the brittle nature of the fracture process along the fiber direction. In long fiber composites, the path of a transverse matrix crack often follows fiber-matrix interfaces as well. Including an additional combined failure path that goes through both the matrix and the fiber-matrix interface (or alternatively replacing the intra-matrix path used in this study with the combined path) within the reduced order model is straightforward. Inclusion of such a path requires defining the interface strength and failure parameters in addition to the bulk matrix fracture properties that are not straightforward to identify using traditional experimental characterization techniques. For purposes of model verification, the path of the transverse matrix cracking mode is taken to go through the matrix phase only.

The elastic and fracture parameters for matrix and fiber employed in the numerical examples are summarized in Table 1. The mode I cohesive strength and energies are 4.87 GPa and 48.72 MPa-mm for fiber fracture, and 84.86 MPa and 4.24 MPa-mm for transverse matrix cracking. Fracture energies employed in this section are relatively large to exacerbate the quasi-brittle behavior and the softening stage, in order to clearly demonstrate mesh size objectivity. Figure 8 shows the mode I traction-separation curves of the constituents generated by the cohesive law described by Section 3.1. The overall traction-separation curve is very similar to a bilinear law, but the present model form allows a smoother transition from the hardening to the linear softening regime.

Table 1: Model parameters for matrix and fiber

Matrix Properties (isotropic)							
E [GPa]	ν	α_1 [MPa $^{-1}$]	α_2 [rad]	K [MPa]			
3.55	0.35	8×10^{-3}	1.57	10^9			
Fiber Properties (transversely isotropic)							
E_1 [GPa]	E_2 [GPa]	G_{12} [GPa]	ν_{12}	ν_{23}	α_1 [MPa $^{-1}$]	α_2 [rad]	K [MPa]
263.00	13.00	27.50	0.32	0.20	1.3×10^{-4}	1.57	10^{10}

4.1.1 Mesh size objectivity

Figure 9 displays the geometry, loading and boundary conditions of the macroscopic domain. The macroscopic specimen is subjected to displacement-controlled loading until failure. In Fig. 9a and 9c, the configurations are perpendicular to the failure paths under uniaxial tension condition resulting in mode I fracture within the matrix and fiber, respectively. Sym-

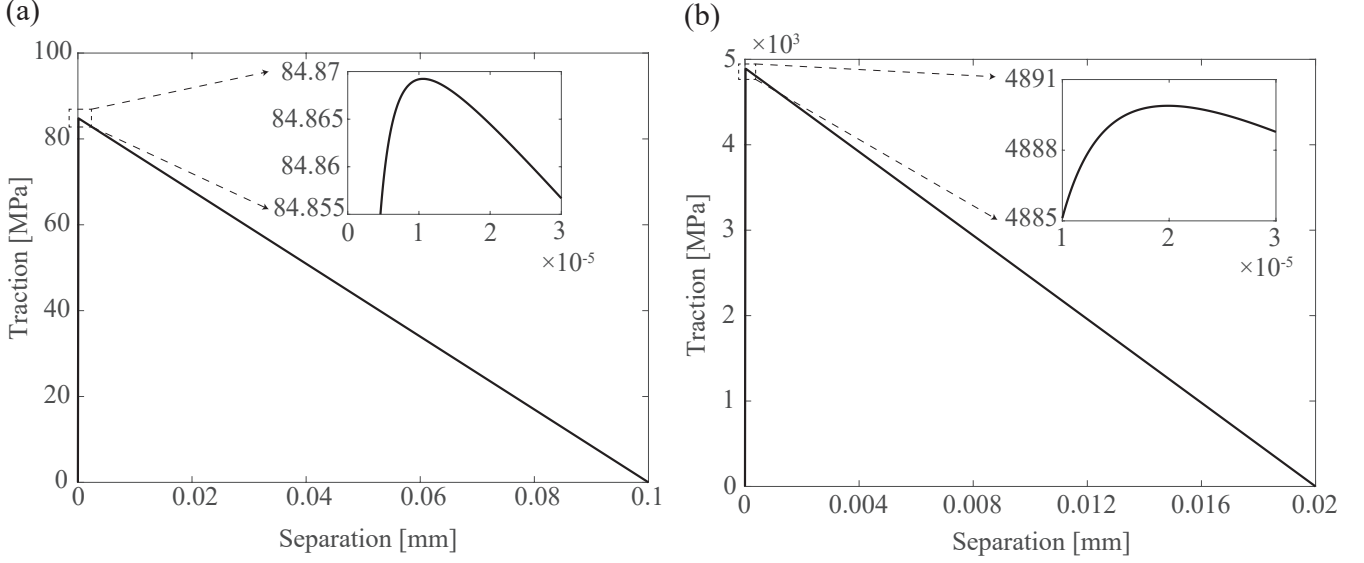


Figure 8: Traction-separation relationship of (a) the matrix constituent (b) the fiber constituent under mode I loading. The inset figures shows close-ups near the ultimate traction

metry boundary conditions are applied to the three sides normal to x, y and z directions. The configuration in Fig. 9b is a simple shear test, in which mesh size sensitivity is studied under mode II fracture conditions. This is achieved by suppressing the possibility of the onset of mode I dominated fracture through the use of single failure path parallel to the shear loading. The inclusion of a failure path oriented at 45 degree angle to the shear loading would enable mode I fracture under simple shear. In order to ensure damage localization in the examples, the properties in one layer of elements along the expected fracture surface (illustrated as dark regions in Fig. 9) have been slightly perturbed. The macroscale domain is discretized using four different element sizes (denoted as h) of 1 mm, 0.5 mm, 0.25 mm, 0.125mm. 8-noded tri-linear hexahedral elements with reduced integration (1 quadrature point per element) and hourglass control are employed in the macroscale discretizations.

Figures 10a-c show the macroscopic stress-strain curves, along with the evolution the critical cohesive damage variable (i.e., $\omega^{(m)}$ or $\omega^{(f)}$) in the localization zones for the three loading configurations shown in Fig. 10. The first two loading configurations result in failure completely dominated by transverse matrix cracking, whereas the last configuration results in fiber fracture dominated failure. In all cases, no appreciable damage accumulation is observed in the non-dominant failure path. The stress-strain curves for the four discretizations are nearly overlapping and the overall softening stiffness in the specimen stays the same regardless of the mesh size in both matrix cracking and fiber fracture dominated cases. In all cases, the macroscopic stress (along with the traction along the dominant failure path within the unit cell) reaches its peak when the cohesive damage variable of the dominant failure path reaches

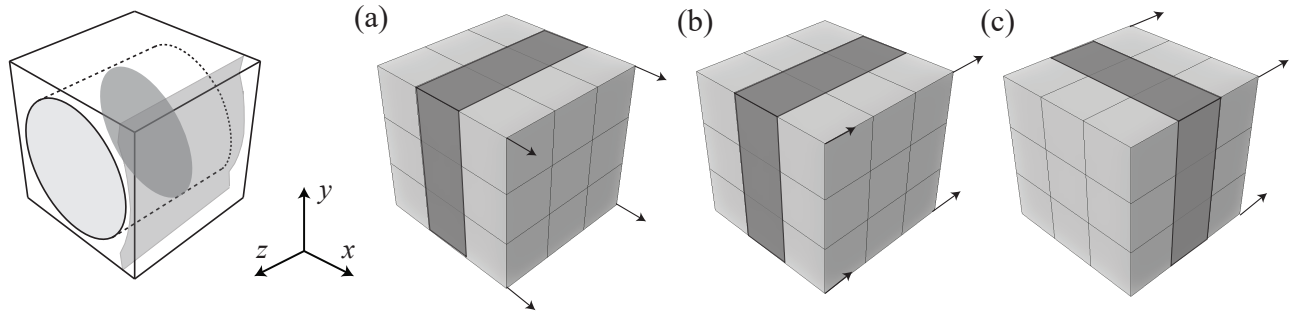


Figure 9: Geometry and loading conditions for the unnotched specimen under (a) matrix cracking dominated mode I condition, (b) matrix cracking dominated mode II condition, (c) fiber fracture dominated mode I condition.

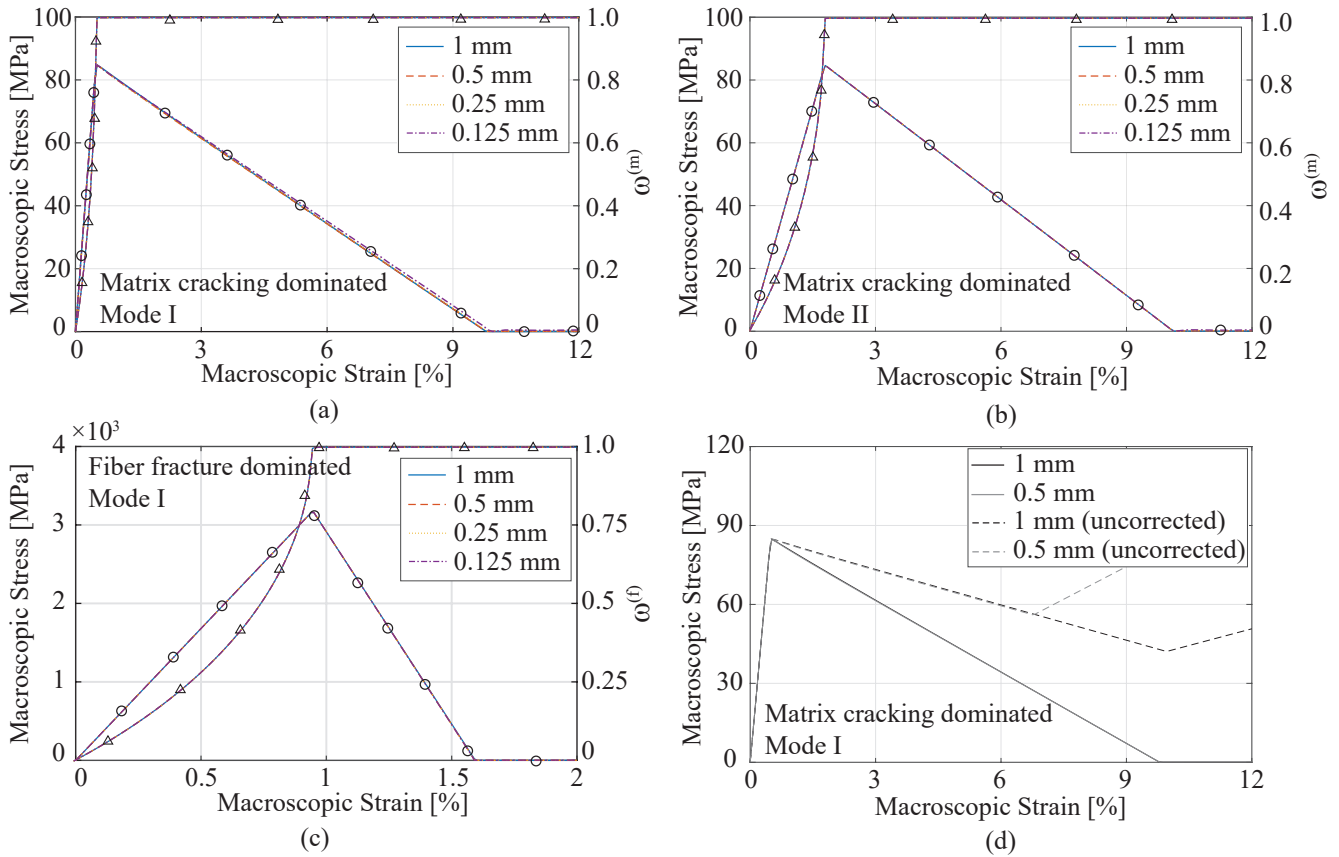


Figure 10: The macroscopic stress-strain curves (denoted by circle mark) and damage evolution (denoted by triangle mark) of unnotched specimen with element size of $h=1$ mm, 0.5 mm, 0.25 mm, 0.125 mm under (a) matrix cracking dominated mode I condition, (b) matrix cracking dominated mode II condition, (c) fiber fracture dominated mode I condition, (d) matrix cracking dominated mode I with and without residual stiffness correction.

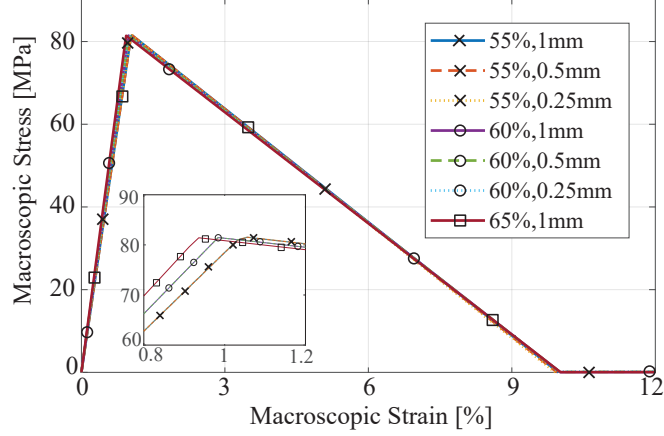


Figure 11: The macroscopic stress-strain curves for unit cells with different fiber volume fractions.

a value slightly lower than unity. Macroscopic stress (and traction along the failure path) vanishes when damage value reaches unity. Figure 10d illustrates the impact of the residual stiffness correction on the resulting macroscopic stress-strain curves. The figure compares those predicted by the $h = 1\text{mm}$ and $h = 0.5\text{mm}$ simulations for matrix dominated failure under uniaxial loading (Fig. 9a). In the absence of residual stiffness correction, a significant residual stiffness is predicted, which gets larger as the mesh is refined. The proposed correction eliminates this spurious effect.

In Fig. 11, mesh size insensitivity of the proposed formulation has been demonstrated for unit cells with different fiber volume fractions subjected to matrix dominated failure under mode I loading as shown in Fig. 9a. Three unit cells with fiber volume fractions of 55%, 60% and 65% were considered. The simulations demonstrate that the behavior is mesh size independent for all values of fiber volume fraction. Only small discrepancies have been observed between the specimens with different fiber volume fractions. The macroscopic stiffnesses are 7.85 GPa, 8.28 GPa, and 8.73 GPa for 55%, 60% and 65% configurations, respectively. The ultimate macroscopic strengths and strains to failure are largely unaffected by the fiber volume fractions within the range of values considered. This is because the failure is dictated by the matrix properties, and the overall traction state that the matrix failure path undergoes is not significantly affected by the change in the fiber volume fraction.

The proposed model has been verified by comparing the model predictions with direct numerical simulations of fully resolved microstructure. Abaqus in-built cohesive zone model (CZM) is employed as the reference. The unnotched specimen with the same geometry and failure path conditions is considered. The finite element mesh of the unit cell and the failure path modeled using cohesive zone elements are shown in Fig. 13. COH3D8 elements from the Abaqus cohesive element library were used. Maximum nominal stress criterion for damage initiation and linear energy-based damage evolution are employed for traction-separation

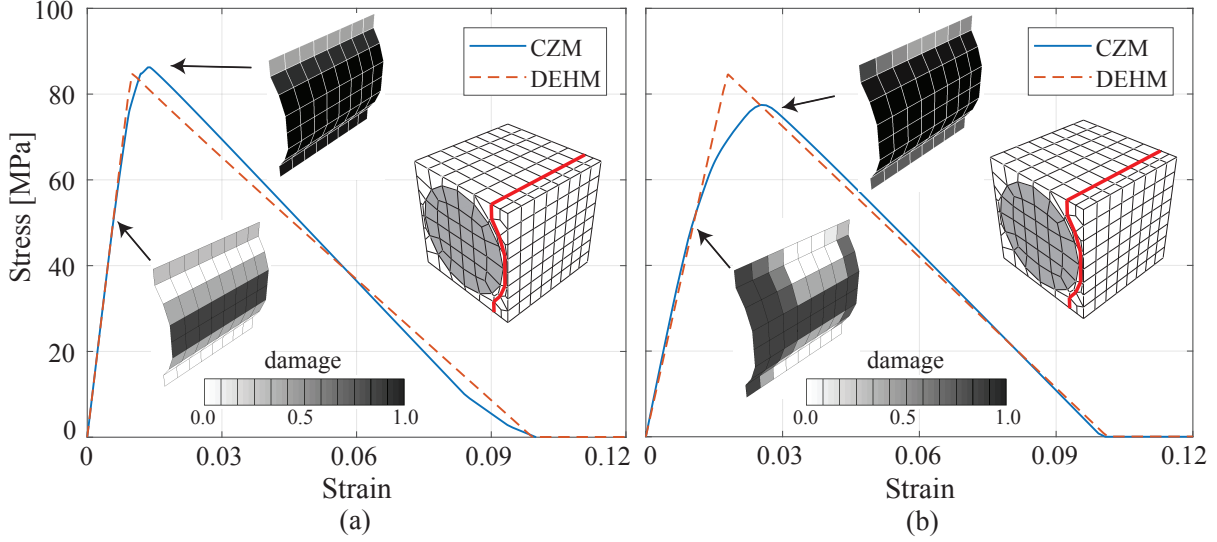


Figure 12: Stress-strain curves predicted by the reference and the proposed approaches, under (a) Mode I condition, and (b) Mode II conditions. Inset contours indicate damage within the cohesive interface.

response of the cohesive element. The stress-strain curves obtained under mode I and II conditions compared with the D-EHM model are shown in Fig. 13. A good overall agreement is observed between the two methods. Damage contours of the cohesive interface demonstrate spatially non-uniform damage evolution. Before reaching the ultimate stress, damage evolves more rapidly in regions closer to the fiber and propagates outward. The -DEHM model approximates spatial evolution of damage as uniform within the failure path. The discrepancies between the reference and proposed models near the peak strength are attributed to this approximation.

4.1.2 Effect of unit cell size and microcrack density

The role of using unit cells with different sizes on the overall macroscopic response is investigated using the unnotched specimen configuration under mode I loading shown in Fig. 9a. Three unit cells (named UC1, UC2 and UC3) shown in Fig. 13a are considered. UC1 is the single fiber square unit cell employed in the verification studies above, whereas UC2 and UC3 are generated by tiling UC1 twice and four times along all directions, respectively. All unit cells consider a single transverse matrix failure path. While the geometric attributes of all three unit cells are identical, the microcrack densities they represent are different. Simulations are performed using $h = 1$ mm over the same macroscale domain (Fig. 9a). ROMs for the unit cells were not regularized to ensure that the crack spacing is not adjusted based on the size scale ratio. The stress-strain curves for the three unit cells are compared in Fig. 13b. The pre-peak response as well as the peak strength predicted by the three configurations are

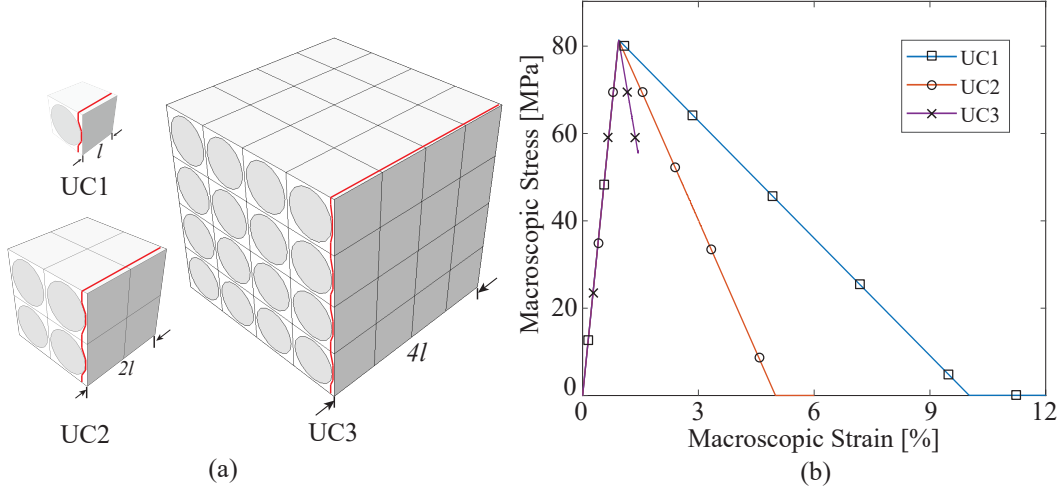


Figure 13: (a) Unit cells with different sizes and microcrack densities, and (b) the corresponding macroscale stress-strain curves.

identical since the behavior is controlled by the geometric attributes of the unit cells in this regime. In the softening regime, the stress-strain response becomes progressively more brittle with increasing unit cell size. This is because, the smaller microstructure with larger crack density dissipates more energy compared with larger microstructures with wider microcrack spacing via progressive loss of cohesion along the microcracks.

4.1.3 Effect of unit cell morphology

Next, we investigate the failure behavior of the composite as a function of the choice of the unit cell and the failure path morphology. The investigations compare the failure behavior in the square unit cell (Fig. 7) to a unit cell with hexagonal fiber arrangement with identical fiber volume fraction (Fig. 14). The use of hexagonal unit cell introduces two complications compared to the square unit cell. Under uni-axial loading, the square unit cell permits the selection of a planar failure path orthogonal to the loading axis (with the smallest possible surface area). In contrast, the failure path in the hexagonal unit cell is necessarily tortuous due to the fiber arrangement. Additionally, hexagonal configuration of the fibers introduces anisotropy evidenced by the higher tortuosity of fracture paths along directions perpendicular to the fibers. The current study focused on characterization of fracture paths along $x-z$ and $y-z$ planes within the matrix constituents of the hexagonal unit cell. In order to understand the role of discretization on the selection of the failure path, five separate paths with near identical surface areas are chosen as illustrated in Fig. 14. The relative surface areas, (normalized by the area of an extended surface of the square unit cell) of the failure paths in the square and hexagonal unit cells are approximately 1 for the square unit cell and 1.5 for the

hexagonal unit cell, respectively. The macroscale discretization consists of a single hexahedron element subjected to uniaxial loading along the transverse direction with displacement control. Figure 15 shows the stress-strain plots produced by different failure path morphologies and unit cells. The stress-strain behavior of the failure paths within the $x-z$ plane of the hexagonal unit cell (Hex FP1, Hex FP2, Hex FP3 and Hex FP4) are nearly identical to each other. This indicates stable response, where perturbations in the choice of fracture path morphology do not result in significant changes in the stress-strain behavior. In addition, failure path Hex FP1 - Hex FP4 result in substantially higher strength (92 MPa) and dissipated energy (6.16 MPa-mm) than square unit cell (85 MPa and 4.2 MPa-mm) and the orthogonal failure path Hex FP5 (79.2 MPa and 3.762 MPa-mm) in the hexagonal unit cell. This is primarily due to larger cross sectional areas (by approximately 50%) of the Hex FP1 - Hex FP4 paths which are highly tortuous to get across the center fiber in the hexagonal unit cell. Additionally, because of the failure path tortuosity, the fracture path turns away from pure Mode I configuration, potentially resulting in higher resistance to crack formation particularly when the constituent materials exhibit high Mode II fracture energy.

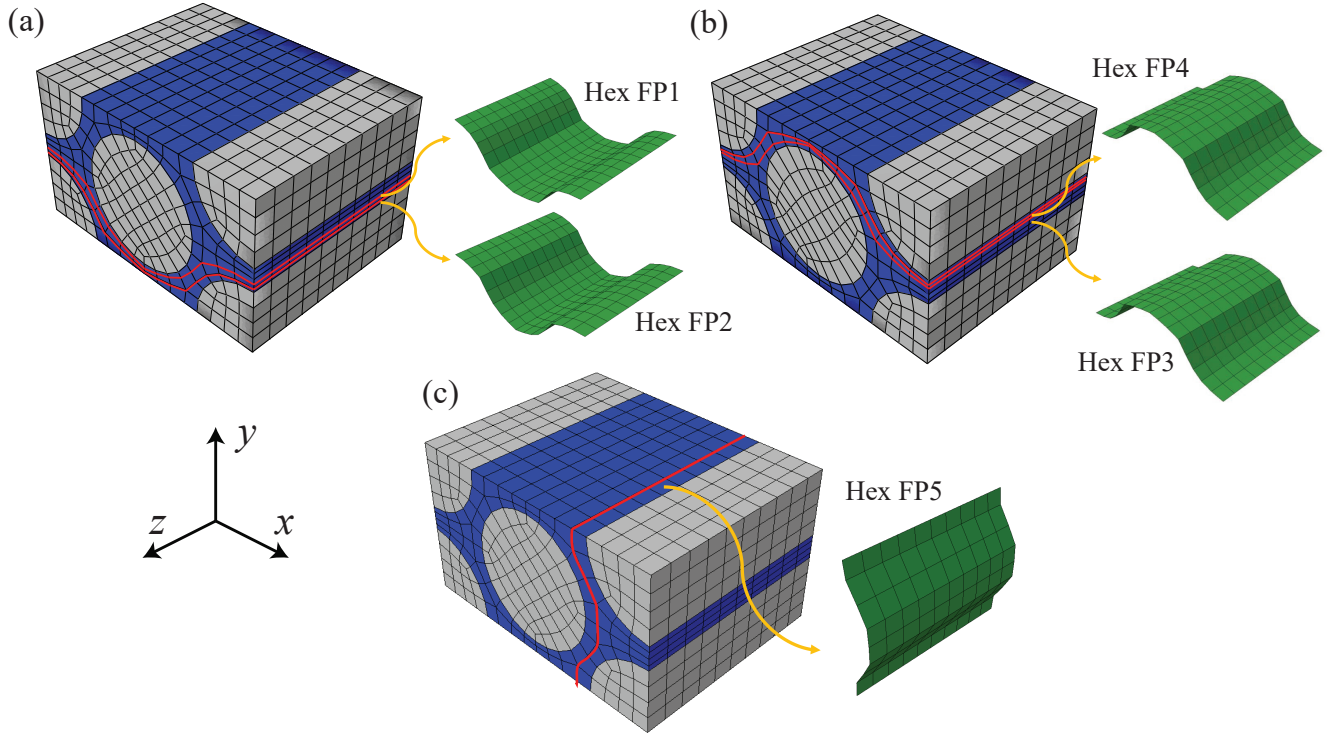


Figure 14: Failure paths in hexagonal unit cells. (a) “Hex FP1”, “Hex FP2” along $x-z$ plane (b) “Hex FP3”, “Hex FP4” along $x-z$ plane (c) “Hex FP5” along $y-z$ plane.

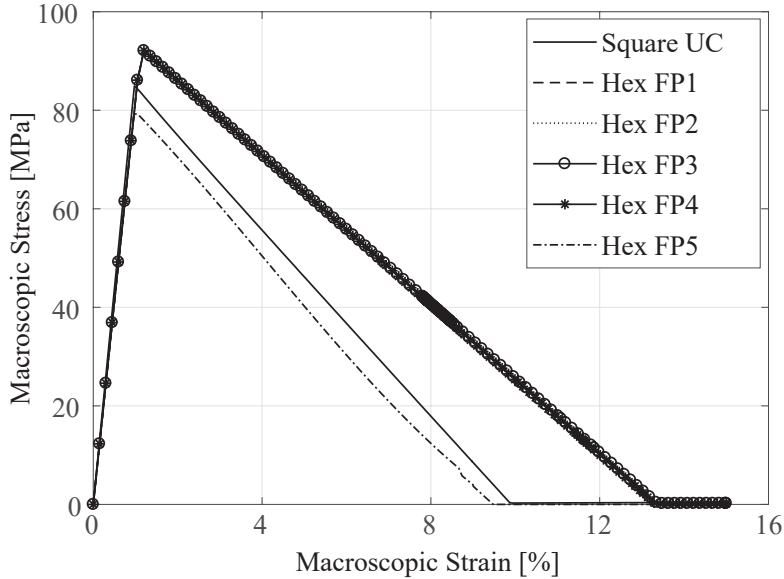


Figure 15: Stress-strain curves of hexagonal and square unit cell configurations.

4.2 Open-hole laminate analysis

The capabilities of the D-EHM approach are further assessed using two open-hole laminated composite configurations. Figure 16a shows the geometry, loading and boundary conditions of a 90° (i.e., the fibers are oriented along the z -direction) single-ply lamina specimen. The reduced order model shown in Fig. 7 that includes matrix cracking and fiber fracture paths is employed in this section. The overall dimensions of the specimen are 38mm, 80mm and 0.125mm in width, length and thickness, respectively. The radius of the hole is 3.175mm. Symmetry boundary conditions are applied at the three sides and 1/8 of the specimen is modeled. The domain is subjected to displacement-controlled uniaxial tension loading. The model parameters and the corresponding fracture properties for the fiber and matrix materials are shown in Table 2. The resulting mode I cohesive strength and energies for fiber fracture are 3.97 GPa and 12.57 MPa-mm, and for transverse matrix cracking are 84.75 MPa and 0.27 MPa-mm. The values for the strength of the fiber, and the strength and fracture energy of the matrix are generally consistent with generic unidirectionally carbon fiber reinforced thermoset composites. While the fracture energy for the fiber is not easy to obtain experimentally and generally considered purely brittle, new experimental studies point to quasi-brittle behavior for fiber as well (see Ref. [54]). Under the applied loading and geometry conditions, fracture in the specimen is expected to initiate near the hole in the form of matrix cracking and propagate as mode I dominated fracture. In order to ensure that the mesh alignment does not impede crack propagation, the domain of the specimen around the notch is discretized using structured meshes aligned with the fiber direction. The sizes of $h=0.5\text{mm}$, 0.25mm , 0.125mm , 0.0625mm ,

and 0.03125mm are used in the structured portion of the mesh (see Fig. 16b-f). For all the meshes, there is single element discretization per ply in the thickness direction.

Table 2: Fracture process parameters used in the open-hole simulations

Matrix Failure						
G_{Ic}	G_{IIc}	t_{ult}	α_1	α_2	K_I	K_{II}
[MPa mm]	[MPa mm]	[MPa]	[MPa ⁻¹]	[rad]	[MPa]	[MPa]
0.27	0.98	84.75	7.5×10^{-3}	1.57	10^5	2.8×10^8
Fiber Failure						
G_{Ic}	G_{IIc}	t_{ult}	α_1	α_2	K_I	K_{II}
[MPa mm]	[MPa mm]	[MPa]	[MPa ⁻¹]	[rad]	[MPa]	[MPa]
12.57	12.57	3967.82	1.6×10^{-4}	1.57	10^{10}	10^{10}

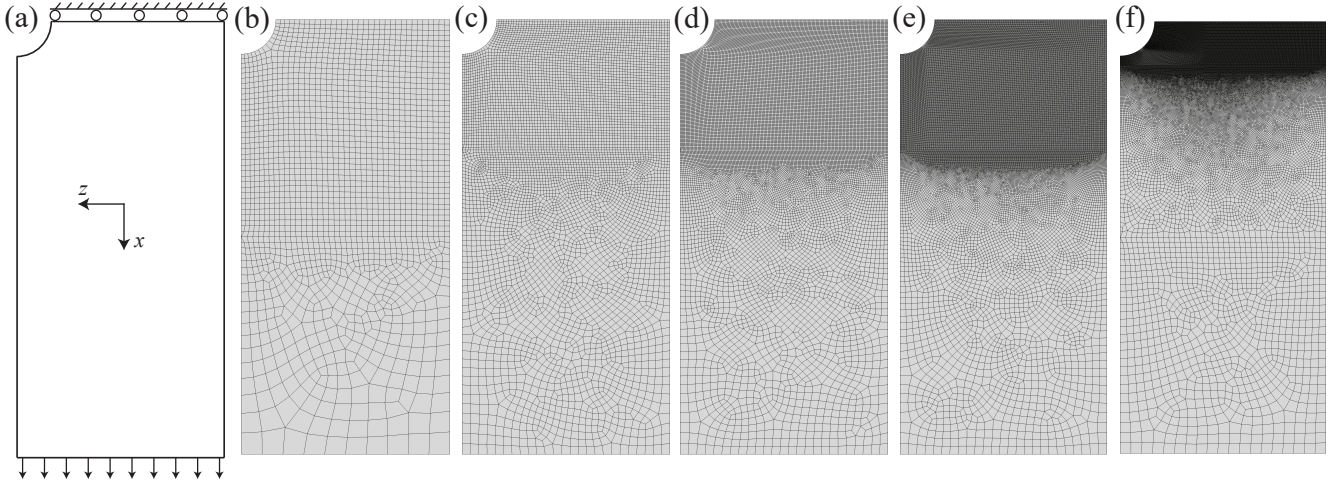


Figure 16: (a) Geometry, loading and boundary conditions for open-hole configuration. Mesh discretizations of (b) $h=0.5$ mm, (c) $h=0.25$ mm, (d) $h=0.0625$ mm, (e) $h=0.03125$ mm.

Figure 17 compares the transverse matrix damage contours and crack propagation paths predicted using three different discretizations ($h=0.25$ mm, 0.125mm, 0.0625mm) at the exact same stage of the loading process. The other two discretizations show the same pattern of response. In the figure, the crack is displayed by removing the elements which have reached complete damage state ($\omega^{(m)} = 1$) during the post processing stage. Element erosion is not employed in the simulations. The damage contours show that damage nucleates at the brim of the hole, followed by the crack initiation and extension along the fiber direction. The simulation results show that a damage process zone forms near the notch followed by

rapid propagation of the transverse matrix crack. Both the process zone as well as the crack propagation are independent of the element size employed in the discretization. Figure 18a shows the force-displacement curves generated by various mesh densities. The formation of the damage process zone around the notch occurs during the hardening stage. Near the onset of crack nucleation (when damage in the transverse matrix crack path reaches unity in the first element), the force-displacement curve reaches peak. The crack propagation occurs as the force-displacement curve undergoes vertical drop. Despite the brittle nature of the structural cracking, the crack propagation phase is well-resolved using the proposed approach. This is evidenced by the fine resolution of the force drop in all simulations. The structural stiffness and strength is consistently predicted using the proposed approach with different mesh resolution (see inset in Fig. 18a). The mesh size insensitivity is further evidenced in Fig. 18b that shows the failure strength as a function of element size. The mean predicted value is 45 MPa, the standard deviation of 0.5 MPa.

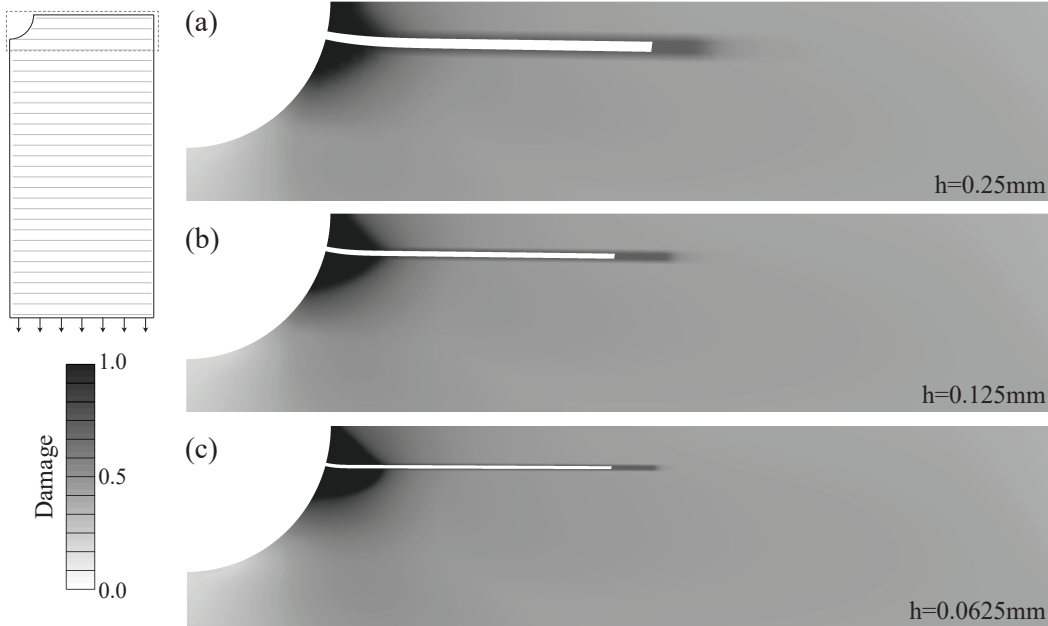


Figure 17: Transverse matrix damage ($\omega^{(m)}$) contours and crack propagation in 90° open-hole specimens with three element sizes of (a) $h=0.25$ mm, (b) $h=0.125\text{mm}$, (c) $h=0.0625\text{mm}$.

Next, we demonstrate the capabilities of the proposed approach in a laminate configuration that results in more complex failure patterns. We study a $[0^\circ/90^\circ]_S$ laminate that includes four plies along the thickness direction. Only two of the plies were modeled exploiting symmetry in the thickness direction. The remaining geometrical, loading and mesh configurations are set identical to those of the 90° lamina example described above. The damage contours within the zero and ninety plies predicted by three mesh sizes (i.e. $h=0.25\text{mm}$, 0.125mm , 0.0625mm) at the exact same stage of the loading process are shown in Fig. 19. In the 0° ply, both fiber

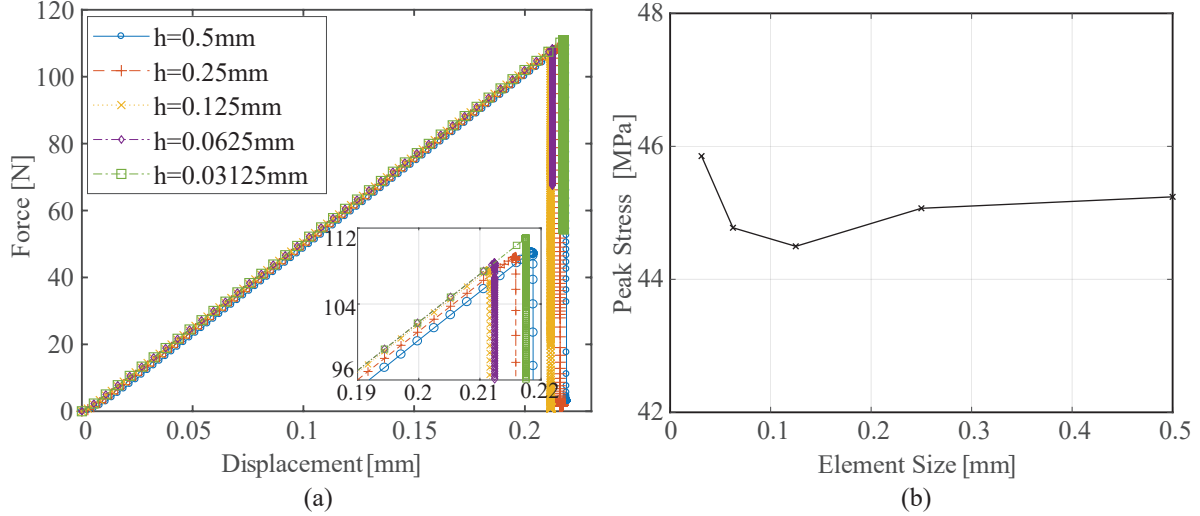


Figure 18: (a) Force-displacement curves of the 90° open-hole specimens, (b) Peak (ultimate) strength as a function of element size.

and matrix damage are observed, which nucleate at the notch. Fiber crack propagation is the critical mode and determines the strength of the structure. Before the nucleation of fiber fracture, the matrix damage forms a process zone near the notch and transverse matrix crack propagates along the vertical direction parallel to loading (i.e., splitting). The length of the split is approximately twice the radius of the hole. The lines (identified as red on the electronic version of the manuscript) in the figures are included to indicate the orientation of the matrix cracks and not a part of the simulations. The fiber crack then initiates and quickly propagates along the lateral direction. In the 90° layer, no fiber damage is observed. Fig. 19c shows the contours of matrix damage, which extends around the axial splits formed by the matrix damage in the 0° ply. The matrix damage in both plies form and propagate at approximately the same stages of loading. The pattern of damage contours described above matches well with those experimentally observed in specimens with similar laminate configurations (See e.g. Ref. [55]). No significant delamination occurs in $[0^\circ/90^\circ]$ cross-ply configurations. It is important to note that there are no significant differences between the failure patterns predicted by different discretizations, pointing to the mesh size insensitivity of the proposed approach, even in more complex damage propagation cases.

Figure 20 displays the force-displacement curves predicted by the five discretizations, as well as the variation of the peak strength of the laminate as a function of element size. Similar to the 0° lamina case, the D-EHM approach captures the crack propagation stage in the cross ply laminate. There is a very good agreement in strength predictions of different discretizations. The mean strength is 805 MPa with a standard deviation of 9 MPa.

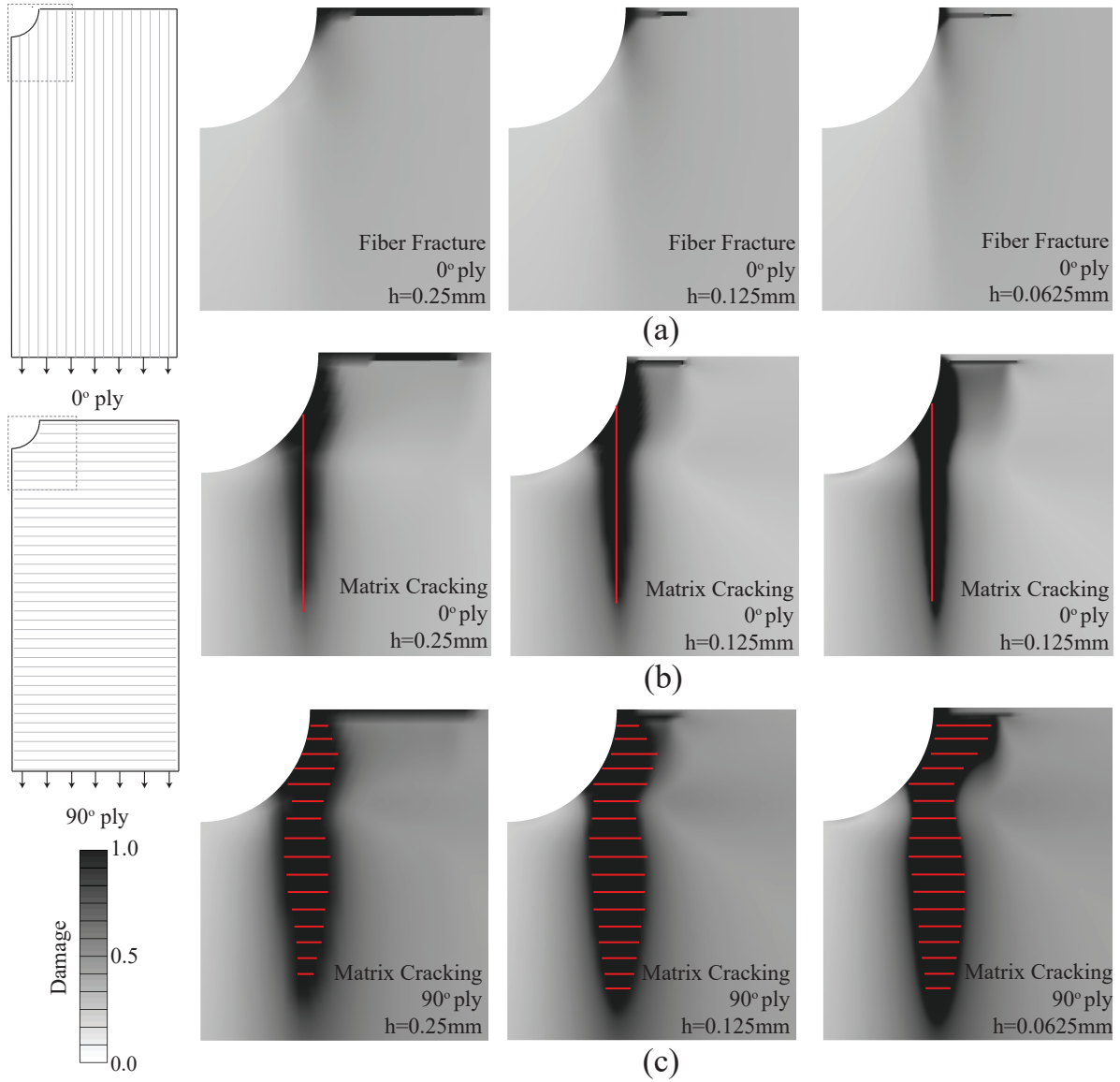


Figure 19: Damage contours and crack propagation for (a) fiber fracture in 0° ply, (b) matrix cracking in 0° ply, (c) matrix cracking in 90° ply, in $[0^\circ/90^\circ]_S$ open-hole specimens with three element sizes of $h=0.25$ mm, 0.125mm , and 0.0625mm .

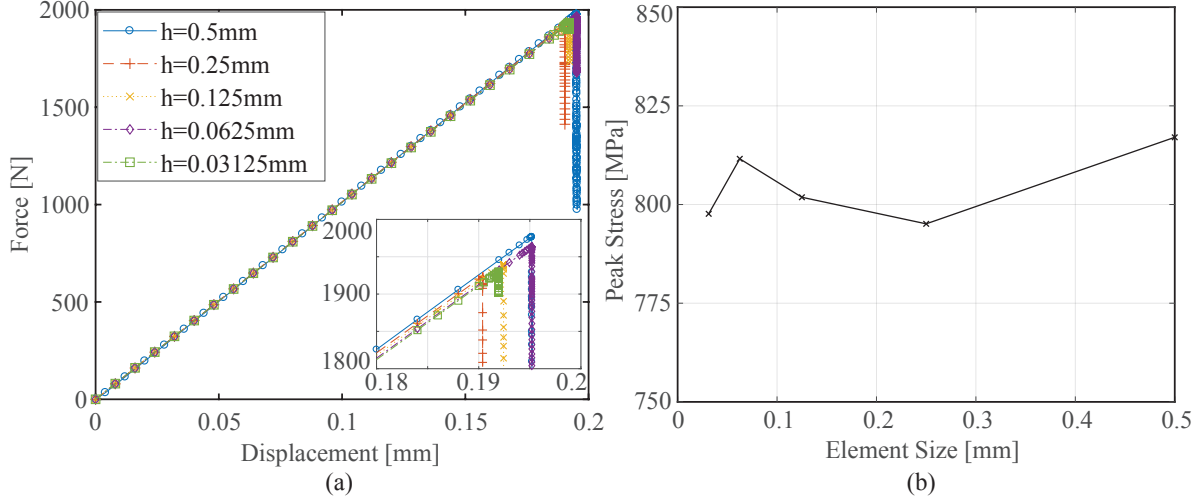


Figure 20: (a) Force-displacement curves of $[0^\circ/90^\circ]_S$ lamina, (b) Peak (ultimate) strength as a function of element size.

5 Conclusions

This manuscript presented a new computational homogenization method to study the behavior of composite materials undergoing failure. The proposed approach offers a reduced order representation of the fracture process at the scale of the material microstructure, which allows orders of magnitude computational efficiency compared with the existing CH formulations. The proposed formulation achieves mesh size objectivity by employing the concept of macroscale element size-dependent microstructure volume. The mesh size objective formulation is achieved in an “effective” manner through analytical formulae that scales the reduced order model coefficients as a function of the macroscale element size. The capabilities of the proposed multiscale approach has been demonstrated in the context of 3-D laminated composite specimen configurations subjected to tensile loading. Numerical studies point to mesh size independence, as well as accurate treatment of simultaneous presence and growth of multiple mechanisms of failure including matrix damage and fiber fracture.

The proposed approach will be extended and generalized in a number of respects. The role of microstructural features, microstructure morphology and failure path discretization on the overall failure prediction of composite specimens will be further investigated. Additional failure mechanisms (e.g., compression, fatigue) will be incorporated to extend the applicability of the proposed approach to a broader array of failure problems. Furthermore, despite alleviating mesh size sensitivity, the proposed approach does not address the important issue of mesh bias – the propensity of macroscale cracks to follow mesh lines. The present formulation will be extended to alleviate the mesh bias issue.

6 Acknowledgements

The authors gratefully acknowledge the financial support of the Office of Naval Research Airframe Structures and Materials (Award No: N00014-17-1-2040, Program Manager: William C. Nickerson) and the Air Force Research Laboratory (Contract No: FA8650-12-D-3212/0016 under University of Dayton Research Institute Subcontract No. RSC16122, Program Managers: Dr. Steven E. Olson and Dr. Stephen B. Clay).

References

- [1] W. E. W. B. E. Engquist, and Z. Huang. Heterogeneous multiscale method: A general methodology for multi-scale modeling. *Phys. Rev. B*, 67(9):92–101, 2003.
- [2] Y. Efendiev and T. Y. Hou. *Multiscale Finite Element Methods*. Springer, 2009.
- [3] C. Oskay. Variational multiscale enrichment method with mixed boundary conditions for modeling diffusion and deformation problems. *Comput. Methods Appl. Mech. Engrg.*, 264: 178–190, 2013.
- [4] S. Zhang and C. Oskay. Variational multiscale enrichment method with mixed boundary conditions for elasto-viscoplastic problems. *Comput. Mech.*, 55:771–787, 2015.
- [5] T. J. R. Hughes, G. R. Feijoo, and J. B. Quincy. The variational multiscale method - a paradigm for computational mechanics. *Comp. Meth. Appl. Mech. Engrg.*, 166:3–24, 1998.
- [6] T. Arbogast. Analysis of a Two-Scale, Locally Conservative Subgrid Upscaling for Elliptic Problems. *SIAM Journal on Numerical Analysis*, 42:576, 2004.
- [7] J. M. Guedes and N. Kikuchi. Preprocessing and postprocessing for materials based on the homogenization method with adaptive finite element methods. *Comput. Meth. Appl. Mech. Engrg.*, 83:143–198, 1990.
- [8] K. Terada and N. Kikuchi. Nonlinear homogenization method for practical applications. In S. Ghosh and M. Ostoja-Starzewski, editors, *Computational Methods in Micromechanics*, volume AMD-212/MD-62, pages 1–16. ASME, 1995.
- [9] I. M. Gitman, H. Askes, and L. J. Sluys. Representative volume: Existence and size determination. *Eng. Fract. Mech.*, 74:2518–2534, 2007.

- [10] K. Matous, M. G. Kulkarni, and P. H. Geubelle. Multiscale cohesive failure modeling of heterogeneous adhesives. *J. Mech. Phys. Solids*, 56:1511 – 1533, 2008.
- [11] C. B. Hirshberger, N. Sukumar, and P. Steinmann. Computational homogenization of material layers with micromorphic mesostructure. *Phil. Mag.*, 88:3603–3631, 2008.
- [12] T. B. Belytschko, S. Loehnert, and J. H. Song. Multiscale aggregating discontinuities: a method for circumventing loss of material stability. *Int. J. Numer. Meth. Engng.*, 73: 869–894, 2008.
- [13] C. V. Verhoosel, J. J. C. Remmers, M. A. Gutiérrez, and R. de Borst. Computational homogenization for adhesive and cohesive failure in quasi-brittle solids. *Int. J. Numer. Meth. Engng.*, 83:1155–1179, 2010.
- [14] V. P. Nguyen, O. Lloberas-Valls, M. Stroeve, and L. J. Sluys. Computational homogenization for multiscale crack modeling implementational and computational aspects. *Int. J. Numer. Meth. Eng.*, 2011. doi: 10.1002/nme.3237.
- [15] V. P. Nguyen, O. Lloberas-Valls, M. Stroeve, and L. J. Sluys. Homogenization-based multiscale crack modelling: From micro-diffusive damage to macro-cracks. *Comput. Meth. Appl. Mech. Engrg.*, 200:1220 – 1236, 2011.
- [16] E. W. C. Coenen, V. G. Kouznetsova, and M. G. D. Geers. Multi-scale continuous–discontinuous framework for computational-homogenization–localization. *J. Mech. Phys. Solids*, 60:1486–1507, 2012.
- [17] E. Bosco, V. G. Kouznetsova, E. W. C. Coenen, M. G. D. Geers, and A. Salvadori. A multiscale framework for localizing microstructures towards the onset of macroscopic discontinuity. *Comput. Mech.*, 54:299–319, 2014.
- [18] P.J. Sanchez, P.J. Blanco, A.E. Huespe, and R.A. Feijóo. Failure-oriented multi-scale variational formulation: Micro-structures with nucleation and evolution of softening bands. *Comput. Meth. Appl. Mech. Engrg.*, 257:221 – 247, 2013.
- [19] S. Toro, P.J. Sánchez, A.E. Huespe, S.M. Giusti, P.J. Blanco, and R.A. Feijóo. A two-scale failure model for heterogeneous materials: numerical implementation based on the finite element method. *International Journal for Numerical Methods in Engineering*, 97 (5):313–351, Oct 2013.
- [20] G. Pijaudier-Cabot and Z. P. Bazant. Nonlocal damage theory. *J. Eng. Mech.*, 113: 1512–1533, 1987.

- [21] M. G. D. Geers, R. de Borst, W. A. M. Brekelmans, and R. H. J. Peerlings. Strain-based transient-gradient damage model for failure analyses. *Comput. Methods. Appl. Mech. Engrg.*, 160:133–153, 1998.
- [22] V. Kouznetsova, M. G. D. Geers, and W. A. M. Brekelmans. Multi-scale constitutive modelling of heterogeneous materials with a gradient-enhanced computational homogenization scheme. *Int. J. Numer. Meth. Engrg.*, 54:1235–1260, 2002.
- [23] J. Oliver, M. A. Caicedo, E. Roubin, A. E. Huespe, and J. A. Hernandez. Continuum approach to computational multiscale modeling of propagating fracture. *Comput. Meth. Appl. Mech. Engrg.*, 294:384–427, 2015.
- [24] I. M. Gitman, H. Askes, and L.J. Sluys. Coupled-volume multi-scale modelling of quasi-brittle material. *European Journal of Mechanics - A/Solids*, 27:302 – 327, 2008.
- [25] M. J. Bogdanor, S. Mahadevan, and C. Oskay. Uncertainty quantification in damage modeling of heterogeneous materials. *Int. J. Mult. Comp. Eng.*, 11:289–307, 2013.
- [26] M. J. Bogdanor, C. Oskay, and S. B. Clay. Multiscale modeling of failure in composites under model parameter uncertainty. *Comput. Mech.*, 56:389–404, 2015.
- [27] S. Zhang and C. Oskay. Hybrid multiscale integration for directionally scale separable problems. *Int. J. Numer. Meth. Engrg.*, 113:1755–1778, 2018.
- [28] J. Aboudi, S. M. Arnold, and Bednarczyk. B. A. *Micromechanics of Composite Materials. A Generalized Multiscale Analysis Approach*. Elsevier, Amsterdam, 2013.
- [29] J. Yvonnet and Q.-C. He. The reduced model multiscale method (R3M) for the non-linear homogenization of hyperelastic media at finite strains. *J. Comput. Phys.*, 223:341–368, 2007. ISSN 0021-9991. doi: 10.1016/j.jcp.2006.09.019.
- [30] M. Cremonesi, D. Neron, P. A. Guidault, and P. Ladeveze. A pgd-based homogenization technique for the resolution of nonlinear multiscale problems. *Comput. Meth. Appl. Mech. Engrg.*, 267:275–292, 2013.
- [31] H. Moulinec and P. Suquet. A numerical method for computing the overall response of nonlinear composites with complex microstructure. *Comput. Meth. Appl. Mech. Engrg.*, 157:69–94, 1998.
- [32] G. J. Dvorak and J. Zhang. Transformation field analysis of damage evolution in composite materials. *J. Mech. Phys. Solids*, 49:2517–2541, 2001.

- [33] J. C. Michel and P. Suquet. Computational analysis of nonlinear composite structures using the nonuniform transformation field analysis. *Comput. Meth. Appl. Mech. Engrg.*, 193:5477–5502, 2004.
- [34] R. D. Crouch and C. Oskay. Symmetric meso-mechanical model for failure analysis of heterogeneous materials. *Int. J. Mult. Comp. Eng.*, 8:447–461, 2010.
- [35] C. Oskay and J. Fish. Eigendefor-mation-based reduced order homogenization for failure analysis of heterogeneous materials. *Comput. Methods Appl. Mech. Engrg.*, 196:1216–1243, 2007.
- [36] P. A. Sparks and C. Oskay. The method of failure paths for reduced-order computational homogenization. *Int. J. Mult. Comp. Eng.*, 14:515–534, 2016.
- [37] J. Oliver, M. A. Caicedo, A. E. Huespe, J.A. Hernández, and E. Roubin. Reduced order modeling strategies for computational multiscale fracture. *Comput. Meth. Appl. Mech. Engrg.*, 313:560 – 595, 2017.
- [38] M. Mosby and K. Matous. Computational homogenization at extreme scales. *Extreme Mechanics Letters*, 6:68–74, 2016.
- [39] B. Hiriyur, R. S. Tuminaro, H. Waisman, E. Boman, and D. E. Keyes. A quasi-algebraic multigrid approach to fracture problems based on extended finite elements. *SIAM J. Sci. Comput.*, 34:A603–A626, 2012.
- [40] Rahul and S. De. Analysis of the jacobian-free multiscale method (jfmm). *Comput. Mech.*, 56:769–783, 2015.
- [41] A. Benssousan, J. L. Lions, and G. Papanicolaou. *Asymptotic Analysis for Periodic Structures*. North-Holland, Amsterdam, 1978.
- [42] J. Fish and R. Fan. Mathematical homogenization of nonperiodic heterogeneous media subjected to large deformation transient loading. *Int. J. Numer. Meth. Engrg.*, 76:1044–1064, 2008.
- [43] E. W. C. Coenen, V. G. Kouznetsova, and M. G. D. Geers. Novel boundary conditions for strain localization analyses in microstructural volume elements. *Int. J. Numer. Meth. Engrg.*, 90:1–21, 2012.
- [44] M. Grigorovitch and E. Gal. The local response in structures using the embedded unit cell approach. *Comput. Struct.*, 157:189–200, 2015.

- [45] Z. P. Bazant and B. H. Oh. Crack band theory for fracture of concrete. *Materials and Structures*, 16:155–177, 1983.
- [46] A. Pandolfi and M. Ortiz. An eigenerosion approach to brittle fracture. *Int. J. Numer. Meth. Engng.*, 92:694–714, 2012.
- [47] J. Oliver. A consistent characteristic length for smeared cracking models. *Int. J. Numer. Meth. Engng.*, 28:461–474, 1989.
- [48] M. Jirasek and M. Bauer. Numerical aspects of the crack band approach. *Comput. Struct.*, 110-111:60–78, 2012.
- [49] R. Furuhashi and T. Mura. On the equivalent inclusion method and impotent eigenstrains. *J. Elasticity*, 9:263–270, 1979.
- [50] J. Fish, V. Filonova, and Z. Yuan. Hybrid impotent–incompatible eigenstrain based homogenization. *Int. J. Numer. Meth. Engng.*, 95:1–32, 2013.
- [51] M. J. Bogdanor and C. Oskay. Prediction of progressive damage and strength of im7/977-3 composites using the eigendeformation-based homogenization approach: Static loading. *J. Composite Mater.*, 51:1455–1472, 2017.
- [52] M. J. Bogdanor and C. Oskay. Prediction of progressive fatigue damage and failure behavior of im7/977-3 composites using the reduced-order multiple space-time homogenization approach. *J. Composite Mater.*, 51:2101–2117, 2017.
- [53] X. Zhang and C. Oskay. Polycrystal plasticity modeling of nickel-based superalloy in 617 subjected to cyclic loading at high temperature. *Modelling Simul. Mater. Sci. Eng.*, 24 (055009), 2016.
- [54] Marco Salviato, Viet T Chau, Weixin Li, Zdeněk P Bažant, and Gianluca Cusatis. Direct testing of gradual postpeak softening of fracture specimens of fiber composites stabilized by enhanced grip stiffness and mass. *Journal of Applied Mechanics*, 83(11):111003, 2016.
- [55] R. M. O’Higgins, M. A. McCarthy, and C. T. McCarthy. Comparison of open hole tension characteristics of high strength glass and carbon fibre-reinforced composite materials. *Compos. Sci. Technol.*, 68:2770–2778, 2008.

Appendix

In this appendix, we derive the general equations for the scaling of the coefficient tensors. In the case of a single failure path subjected to mode I loading (the same case considered in Section 2.3), the only nonzero component of the separation coefficients is the normal one $\boldsymbol{\delta} = \{\delta_N, 0, 0\}^T$. The corresponding homogenized strain tensor is expressed as:

$$\bar{\boldsymbol{\epsilon}} = \hat{\epsilon}_N \mathbf{n} \otimes \mathbf{n} + \hat{\epsilon}_{S_1} \mathbf{s}_1 \otimes \mathbf{s}_1 + \hat{\epsilon}_{S_2} \mathbf{s}_2 \otimes \mathbf{s}_2 \quad (\text{A1})$$

where \mathbf{n} , \mathbf{s}_1 and \mathbf{s}_2 are basis vectors of local coordinates along with the failure path. The tensor components are all expressed in the local coordinates. Note that Section 2.3 ignored the presence of the latter two terms.

With $\mathfrak{R}_\xi = \mathfrak{R}(\Theta_\xi, S_\xi; \mathbf{C}, \mathbf{D}_\xi, \mathbf{Z}_\xi)$ defined by microstructure with size scale ratio ξ , the weak equilibrium equation (Eq. 17) and the macroscopic constitutive relationship (Eq. 31) are:

$$[(1 - \omega) \mathbf{K} + \mathbf{D}_\xi] \cdot \boldsymbol{\delta} - \mathbf{C} : \bar{\boldsymbol{\epsilon}} = \mathbf{0} \quad (\text{A2})$$

$$\bar{\boldsymbol{\sigma}} = \bar{\mathbf{L}} : \bar{\boldsymbol{\epsilon}} + \mathbf{Z}_\xi \cdot \boldsymbol{\delta} \quad (\text{A3})$$

Substituting the form of the mode I separation coefficient vector and the macro strain state yields (in the indicial notation):

$$[(1 - \omega) K_{i1} + (D_\xi)_{i1}] \delta_N - (C_{i11} \hat{\epsilon}_N + C_{i22} \hat{\epsilon}_{S_1} + C_{i33} \hat{\epsilon}_{S_2}) = 0 \quad (\text{A4})$$

$$\hat{\sigma}_{ij} = \bar{L}_{ij11} \hat{\epsilon}_N + \bar{L}_{ij22} \hat{\epsilon}_{S_1} + \bar{L}_{ij33} \hat{\epsilon}_{S_2} + (Z_\xi)_{ij1} \delta_N \quad (\text{A5})$$

Since $K_{21} = 0$, $K_{31} = 0$ and setting $i = 2, 3$ in Eq. A4, $\hat{\epsilon}_{S_1}$ and $\hat{\epsilon}_{S_2}$ are expressed in terms of $\hat{\epsilon}_N$ and δ_N :

$$\hat{\epsilon}_{S_1} = \nu_1 \hat{\epsilon}_N + \mu_1(\xi) \delta_N \quad (\text{A6})$$

$$\hat{\epsilon}_{S_2} = \nu_2 \hat{\epsilon}_N + \mu_2(\xi) \delta_N \quad (\text{A7})$$

where ν_1 , ν_2 , $\mu_1(\xi)$ and $\mu_2(\xi)$ are:

$$\nu_1 = -\frac{C_{211} C_{333} - C_{311} C_{233}}{C_{222} C_{333} - C_{322} C_{233}} \quad (\text{A8})$$

$$\nu_2 = -\frac{C_{211} C_{322} - C_{311} C_{222}}{C_{233} C_{322} - C_{333} C_{222}} \quad (\text{A9})$$

$$\mu_1(\xi) = \frac{(D_\xi)_{21} C_{333} - (D_\xi)_{31} C_{233}}{C_{222} C_{333} - C_{322} C_{233}} \quad (\text{A10})$$

$$\mu_2(\xi) = \frac{(D_\xi)_{21}C_{322} - (D_\xi)_{31}C_{222}}{C_{233}C_{322} - C_{333}C_{222}} \quad (\text{A11})$$

Substituting Eqs. A6 - A11 into Eqs. A4 and A5 yield:

$$[(1 - \omega) K_{11} + D_{\xi n}] \delta_N - C_n \hat{\epsilon}_N = 0 \quad (\text{A12})$$

$$\hat{\sigma}_{11} = E_n \hat{\epsilon}_N + Z_{\xi n} \delta_N \quad (\text{A13})$$

$$\hat{\sigma}_{22} = E_{s_1} \hat{\epsilon}_N + Z_{\xi s_1} \delta_N \quad (\text{A14})$$

$$\hat{\sigma}_{33} = E_{s_2} \hat{\epsilon}_N + Z_{\xi s_2} \delta_N \quad (\text{A15})$$

Each coefficient can be written as:

$$D_{\xi n} = (D_\xi)_{11} - C_{122}\mu_1(\xi) - C_{133}\mu_2(\xi) \quad (\text{A16})$$

$$C_n = -C_{111} - C_{122}\nu_1 - C_{133}\nu_2 \quad (\text{A17})$$

$$E_n = \bar{L}_{1111} - \bar{L}_{1122}\nu_1 - \bar{L}_{1133}\nu_2 \quad (\text{A18})$$

$$E_{s_1} = \bar{L}_{2211} - \bar{L}_{2222}\nu_1 - \bar{L}_{2233}\nu_2 \quad (\text{A19})$$

$$E_{s_2} = \bar{L}_{3311} - \bar{L}_{3322}\nu_1 - \bar{L}_{3333}\nu_2 \quad (\text{A20})$$

$$Z_{\xi n} = (Z_\xi)_{111} - \bar{L}_{1122}\mu_1(\xi) - \bar{L}_{1133}\mu_2(\xi) \quad (\text{A21})$$

$$Z_{\xi s_1} = (Z_\xi)_{221} - \bar{L}_{2222}\mu_1(\xi) - \bar{L}_{2233}\mu_2(\xi) \quad (\text{A22})$$

$$Z_{\xi s_2} = (Z_\xi)_{331} - \bar{L}_{3322}\mu_1(\xi) - \bar{L}_{3333}\mu_2(\xi) \quad (\text{A23})$$

Taking the derivative of Eq. A13 and using Eq. A12, the softening slope of the normal stress-strain relationship $E_\xi^s = \partial \hat{\sigma}_{11} / \partial \hat{\epsilon}_N$ is obtained as:

$$E_\xi^s = E_n + \frac{Z_{\xi n} C_n}{A_n + D_{\xi n}} \quad (\text{A24})$$

where $A_n = \partial t_N / \partial \delta_N$, representing the approximately linear softening of traction-separation relations denoted as $t_N = (1 - \omega) K_{11} \delta_N$. Setting $\xi = 1$ and denoting the corresponding values of $D_{\xi n}$, $Z_{\xi n}$ and E_ξ^s as D_n , Z_n and E^s , respectively:

$$E^s = E_n + \frac{Z_n C_n}{A_n + D_n} \quad (\text{A25})$$

For the purpose of mesh size objectivity as explained in the main text above and as shown in Figure 4, the relationship between E_ξ^s and E^s becomes:

$$E^s \frac{h(l-h)}{l} = \frac{E_n E_\xi^s}{E_n / (l-h) + E_\xi^s / h} \quad (\text{A26})$$

and by substituting the scaling ratio $\xi = l/h$, we obtain:

$$E_\xi^s = \frac{E_n E^s}{\xi E_n + (1 - \xi) E^s} \quad (\text{A27})$$

Considering the forms $D_{\xi n} = \eta_N D_n$ and $Z_{\xi n} = \eta_N Z_n$ for the adjustment of the coefficient tensors in mode I, the scaling parameter η_N can be obtained by substituting Eqs. A24, A25 into A27:

$$\eta_N = \frac{\xi A_n}{A_n + (1 - \xi)(D_n E_n + Z_n C_n) E_n^{-1}} \quad (\text{A28})$$

The above expression is different from the one provided in Section 2.3 in that ν_1 , ν_2 , $\mu_1(\xi)$ and $\mu_2(\xi)$ are introduced to account for the strain triaxiality. In the examples provided in this manuscript, the differences were found to be small.

Next, we extend the derivation of the residual stiffness correction along the same lines. In this case, we set $D_{\xi n} = \eta_N D_n$ and $Z_{\xi n} = \eta_N \eta_N^r Z_n$, where $\tilde{\eta}_N$ and η_N^r respectively stand for the scaling parameters for crack localization and residual stiffness in the normal direction. The softening slope of the normal stress-strain relationship then becomes:

$$E_\xi^s = E_n + \frac{\tilde{\eta}_N \eta_N^r Z_n C_n}{A_n + \eta_N D_n} \quad (\text{A29})$$

At the onset of complete loss of cohesion (i.e., $A_n = 0$), the scaled normal residual stiffness \hat{E}_n^r is expressed as:

$$\hat{E}_n^r(\eta^r) = E_n + \eta_N^r \frac{Z_n C_n}{D_n} \quad (\text{A30})$$

Let E_n^r denote the value of \hat{E}_n^r when $\eta^r = 1$. If we set the correction factor k_N^r for normal residual stiffness: $k_N^r = \hat{E}_n^r / E_n^r$, η_N^r is expressed as:

$$\eta_N^r = -(1 - k_N^r) \frac{D_n E_n}{Z_n C_n} + k_N^r \quad (\text{A31})$$

Similarly, setting $\xi = 1$ enables the normal softening slope to become:

$$E^s = E_n + \frac{\eta_N^r Z_n C_n}{A_n + D_n} \quad (\text{A32})$$

Substituting Eqs. A31, A29, A32 into Eq. A27, $\tilde{\eta}_N$ is expressed as:

$$\tilde{\eta}_N = \frac{\xi A_n}{A + k_N^r (1 - \xi)(D_n E_n + Z_n C_n) E_n^{-1}} \quad (\text{A33})$$

If k_N^r is set to vanish, we observe that $\tilde{\eta}_N = \xi$.

In addition to the mode I condition discussed above, the scaling relationships are derived for mode II condition. In this case, the separation vector is first set to $\boldsymbol{\delta} = \{0, \delta_{S_1}, 0\}^T$. The

corresponding homogenized strain tensor takes the form:

$$\bar{\boldsymbol{\epsilon}} = \begin{bmatrix} 0 & \hat{\gamma}_{ns_1} & \hat{\gamma}_{ns_2} \\ \gamma_{ns_1} & 0 & \hat{\gamma}_{s_1s_2} \\ \hat{\gamma}_{ns_2} & \hat{\gamma}_{s_1s_2} & 0 \end{bmatrix} \quad (\text{A34})$$

The weak equilibrium equation and macroscopic constitutive relationship become:

$$[(1 - \omega) K_{22} + (D_\xi)_{22}] \delta_{S_1} - C_{212} \hat{\gamma}_{ns_1} = 0 \quad (\text{A35})$$

$$\hat{\sigma}_{12} = \bar{L}_{1212} \hat{\gamma}_{ns_1} + (Z_\xi)_{122} \delta_{S_1} \quad (\text{A36})$$

It is important to note that C_{213} , C_{223} , \bar{L}_{1213} and \bar{L}_{1223} are neglected due to the observation that $C_{213} \ll C_{212}$, $C_{223} \ll C_{212}$, $\bar{L}_{1213} \ll \bar{L}_{1212}$, $\bar{L}_{1223} \ll \bar{L}_{1212}$. Considering the form: $(D_\xi)_{22} = \eta_{S_1} D_{22}$ and $(Z_\xi)_{122} = \eta_{S_1} Z_{122}$, the softening shear modulus $G_\xi^s = \partial \hat{\sigma}_{12} / \partial \hat{\gamma}_{ns_1}$ is computed by differentiating Eq. A36 and using Eq. A35:

$$G_\xi^s = \bar{L}_{1212} + \frac{\eta_{S_1} Z_{122} C_{212}}{A_{s_1} + \eta_{S_1} D_{22}} \quad (\text{A37})$$

where, A_{s_1} stands for the softening slope of traction-separation curve in shear direction. Similarly, $\eta_{S_1} = 1$ is ensured when $\xi = 1$. the softening shear modulus therefore becomes:

$$G^s = \bar{L}_{1212} + \frac{Z_{122} C_{212}}{A_{s_1} + \eta_{S_1} D_{22}} \quad (\text{A38})$$

An approximate simple shear case is considered corresponding to mode II condition as shown in Figure 21. The relationship between G_ξ^s and G^s set to achieve mesh size objectivity is given as:

$$G^s \frac{h(l-h)}{l} = \frac{\bar{L}_{1212} G_\xi^s}{\bar{L}_{1212}/(l-h) + G_\xi^s/h} \quad (\text{A39})$$

By substituting Eqs. A37 and A38 to A39, scaling parameter η_{S_1} for mode II can be written as:

$$\eta_{S_1} = \frac{\xi A_{s_1}}{A_{s_1} + (1 - \xi)(D_{22} \bar{L}_{1212} + Z_{122} C_{212}) \bar{L}_{1212}^{-1}} \quad (\text{A40})$$

The residual stiffness correction in mode II follows the same scheme as discussed above for mode I. The scaling parameters $\tilde{\eta}_{S_1}$ and $\eta_{S_1}^r$ corresponding to damage localization and residual stiffness correction are:

$$\tilde{\eta}_{S_1} = \frac{\xi A_{s_1}}{A_{s_1} + k_{s_1}^r (1 - \xi)(D_{22} \bar{L}_{1212} + Z_{122} C_{212}) \bar{L}_{1212}^{-1}} \quad (\text{A41})$$

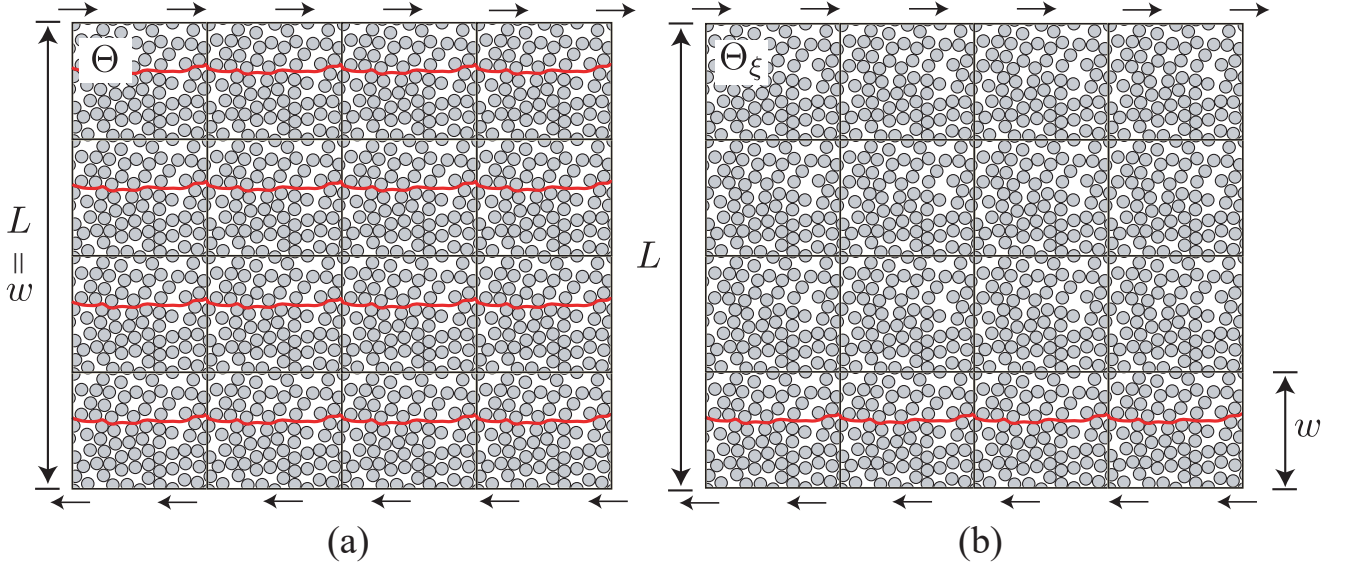


Figure 21: Scaling illustration under approximate simple shear load (a) domain without damage localization represented by repetition of reference microstructure (b) domain with damage localization

$$\eta_{S_1}^r = -(1 - k_{S_1}^r) \frac{D_{22} \bar{L}_{1212}}{Z_{122} C_{212}} + k_{S_1}^r \quad (\text{A42})$$

In the orthogonal direction that excites mode II, the separation coefficient vector is set to $\delta = \{0, 0, \delta_{S_2}\}^T$. The form of scaling relationships are exactly the same as above, only the components of the coefficient tensors are changed in the expressions of scaling parameters:

$$\eta_{S_2} = \frac{\xi A_{s2}}{A_{s2} + (1 - \xi)(D_{33} \bar{L}_{1313} + Z_{133} C_{313}) \bar{L}_{1313}^{-1}} \quad (\text{A43})$$

Extending to residual stiffness correction, scaling parameters $\tilde{\eta}_{S_1}$ and $\eta_{S_1}^r$ corresponding to damage localization and residual stiffness correction are given as:

$$\tilde{\eta}_{S_2} = \frac{\xi A_{s2}}{A_{s2} + k_{S_2}^r (1 - \xi) (D_{33} \bar{L}_{1313} + Z_{133} C_{313}) \bar{L}_{1313}^{-1}} \quad (\text{A44})$$

$$\eta_{S_2}^r = -(1 - k_{S_2}^r) \frac{D_{33} \bar{L}_{1313}}{Z_{133} C_{313}} + k_{S_2}^r \quad (\text{A45})$$

Considering the case that the correction factors $k_{S_1}^r$ and $k_{S_2}^r$ vanish, we obtain the usual classical scaling relationship: $\tilde{\eta}_{S_1} = \tilde{\eta}_{S_2} = \xi$.